Separation and Purification Technology 206 (2018) 208–217

Contents lists available at ScienceDirect

Separation and Purification Technology

journal homepage: www.elsevier.com/locate/seppur

Investigating the non-idealities in adsorption of CO_2-bearing mixtures in cation-exchanged zeolites

Rajamani Krishna[a,*], Jasper M. van Baten[b]

[a] Van 't Hoff Institute for Molecular Sciences, University of Amsterdam, Science Park 904, Amsterdam 1098 XH, The Netherlands
[b] AmsterCHEM, Almería, Spain

ARTICLE INFO

Keywords:
CO_2 capture
Extra-framework cations
Inhomogeneous distribution
Congregation effects
Real adsorbed solution theory

ABSTRACT

Cation-exchanged zeolites have significant potential for capture of CO_2 from a wide variety of mixtures containing N_2, H_2, alkanes and alkenes. The strong coulombic interactions of CO_2 with extra-framework cations result in strong binding and selective capture. Published experimental data on mixture adsorption indicate that the Ideal Adsorbed Solution Theory (IAST) fails to provide accurate estimates of mixture adsorption equilibrium. The reasons for the quantitative failure of IAST estimates are investigated with the aid of Configurational-Bias Monte Carlo (CBMC) simulations of mixture adsorption. Computational snapshots indicate that the failure of the IAST is traceable to inhomogeneous distribution of adsorbates within the zeolite framework.

1. Introduction

Cation-exchanged zeolites are potent adsorbents for selective capture of CO_2 in natural gas purification, flue gas cleaning, and hydrogen purification processes [1–16]. Coulombic interactions of CO_2 with the extra-framework cations result in strong binding; the binding strength and selectivity can be tuned by appropriate choice of the extra-framework cations, and adjustment of the Si/Al ratios [3,13,17], For the design and development of CO_2-capture technologies, that are normally conducted in fixed-bed adsorbers [18–20], the Ideal Adsorbed Solution Theory (IAST) of Myers and Prausnitz [21] is widely used for calculation of mixture adsorption equilibrium [2,8,15,17,22–26].

Briefly, in the IAST, the partial fugacities in the bulk fluid mixture are related to the mole fraction in the adsorbed phase $x_i = \frac{q_i}{q_1+q_2}$ by the analogue of Raoult's law for vapor-liquid equilibrium, i.e. $f_i = P_i^0 x_i$; $i = 1, 2$ where P_i^0 is the pressure for sorption of every component i, which yields the same spreading pressure, π for each of the pure components, as that for the mixture:

$$\frac{\pi A}{RT} = \int_0^{P_1^0} \frac{q_1^0(f)}{f} df = \int_0^{P_2^0} \frac{q_2^0(f)}{f} df \quad (1)$$

The units of $\frac{\pi A}{RT}$, also called the adsorption potential [23,27–29], are mol kg^{-1}. If the *pure* component adsorption $q_i^0(f)$ isotherm are described by, say, the dual-site Langmuir-Freundlich isotherm $q^0(f) = q_{A,sat}\frac{b_A f^{\nu A}}{1+b_A f^{\nu A}} + q_{B,sat}\frac{b_B f^{\nu B}}{1+b_B f^{\nu B}}$, each of the integrals in Eq. (1) can be evaluated analytically. For specified partial fugacities in the bulk fluid phase, f_i, these constraints may be solved simultaneously, to yield the set of values of the adsorbed phase mole fractions, x_i, and P_i^0, all of which must satisfy Eq. (1). The corresponding values of the integrals using these values of P_i^0 as upper limits of integration must yield the same value of $\frac{\pi A}{RT}$ for each component.

A number of experimental data on mixture adsorption equilibrium reveal the IAST does not provide accurate estimates of component loadings, and adsorption selectivities, especially for operations at high guest occupancies [27,29]. As illustration, Fig. 1a,b,c present comparisons of experimental data on adsorption selectivity with IAST estimates for CO_2/CH_4 and CO_2/N_2 mixtures in NaX (trade name = 13X) and LTA-5A zeolites. The IAST selectivity estimates are about an order of magnitude higher than those determined experimentally. The experimental data for selectivity of adsorption of CO_2/C_3H_8 mixtures in 13X, ZSM-5 (Si/Al = 15), and H-MOR zeolites show that the selectivity decreases with increased mole fraction of CO_2 in the bulk gas mixture, $y_1 = \frac{f_1}{f_1+f_2}$. On the other hand, the IAST predicts the selectivity to increase, albeit slightly, with the mole fraction of CO_2 in the bulk gas

* Corresponding author.
E-mail address: r.krishna@contact.uva.nl (R. Krishna).

https://doi.org/10.1016/j.seppur.2018.06.009
Received 24 April 2018; Received in revised form 22 May 2018; Accepted 2 June 2018
Available online 02 June 2018
1383-5866/

Nomenclature

A	surface area per kg of framework, $m^2\ kg^{-1}$
b_i	Langmuir-Freundlich parameter,$Pa^{-\nu}$
C	constant used in Eq. (3), $kg\ mol^{-1}$
f_i	partial fugacity of species i, Pa
f_t	total fugacity of bulk fluid mixture, Pa
p_i	partial pressure of species i, Pa
p_t	total system pressure, Pa
P_i^0	sorption pressure, Pa
q_i	molar loading species of species i, $mol\ kg^{-1}$
$q_{i,sat}$	molar loading of species i at saturation, $mol\ kg^{-1}$
q_t	total molar loading of mixture, $mol\ kg^{-1}$
Q_i	volumetric uptake of species i, $Q_i = \rho q_i$, $mol\ m^{-3}$
ΔQ	separation potential, $mol\ m^{-3}$
R	gas constant, $8.314\ J\ mol^{-1}\ K^{-1}$
S_{ads}	adsorption selectivity, dimensionless
T	absolute temperature, K
x_i	mole fraction of species i in adsorbed phase, dimensionless
y_i	mole fraction of species i in bulk fluid mixture, dimensionless

Greek letters

γ_i	activity coefficient of component i in adsorbed phase, dimensionless
Λ_{ij}	Wilson parameters, dimensionless
ν	Freundlich exponent in unary isotherm, dimensionless
π	spreading pressure, $N\ m^{-1}$
ρ	framework density, $kg\ m^{-3}$

Subscripts

1	referring to species 1
2	referring to species 2
i,j	components in mixture
i	referring to component i
t	referring to total mixture
sat	referring to saturation conditions

Superscripts

0	referring to pure component loading

mixture; see Fig. 1 d,e,f. There are several other examples of failures of the IAST estimations for mixture adsorption in a variety of cation-exchanged zeolites [4,30,31].

The primary objective of this communication is to gain some insights into the reasons for the failure of the IAST to match the experimental data, as witnessed in Fig. 1. Towards this end, Configurational-Bias Monte Carlo (CBMC) simulations on unary isotherms and mixture adsorption equilibrium were performed using the simulation methodology that is firmly established in the literature [6,7,32–34]. The force field information are taken from García-Sanchez et al.[35], and Dubbeldam et al.[36].

The Supplementary Material accompanying this publication provides (a) details of experimental data and CBMC simulation data for mixture adsorption, (b) unary isotherm fits for all the guest/host combinations examined in this article, (c) details of the IAST, and Real Adsorbed Solution Theory (RAST) methodologies and calculations for mixture adsorption equilibrium, and (d) Wilson parameter fits for thermodynamic non-idealities.

2. CBMC simulations of mixture adsorption in cation-exchanged FAU zeolites

We first investigate $CO_2(1)/C_3H_8(2)$ mixture adsorption in NaX zeolite, that has the Faujasite (FAU) topology consisting of cages of 786 $Å^3$ volume, separated by 7.3 Å 12-ring windows. Each unit cell of NaX zeolite has 106 Si, 86 Al, 86 Na^+ with Si/Al = 1.23. Two different CBMC simulation campaigns were conducted:

(i) The mole fraction of $CO_2(1)$ in the bulk gas phase is held constant, $y_1 = 0.5$, and the bulk gas phase fugacity $f_t = f_1 + f_2$ was varied, and
(ii) The mole fraction of $CO_2(1)$ in the bulk gas phase, y_1 was varied from 0 to 1, keeping the bulk gas phase mixture fugacity $f_t = f_1 + f_2$ constant at a value of 1 MPa.

The results of these two separate campaigns are presented in Fig. 2. In the Henry regime of adsorption, prevailing at $f_t < 10$ kPa, the component loadings of CO_2, and C_3H_8 are nearly equal to each other (cf. Fig. 2a), and the $CO_2(1)/C_3H_8(2)$ adsorption selectivity, S_{ads}, is close to unity (cf. Fig. 2b). With increasing values of the bulk gas phase fugacity f_t, above about 100 kPa, the adsorption becomes increasingly in favor of CO_2, due to strong Coulombic interactions with the extra-framework Na^+ cations. The IAST estimates for the adsorption selectivity are plotted as dashed lines in Fig. 2b. At $f_t = 1$ MPa, the value of $S_{ads} \approx 4$; the IAST estimate is a factor two higher than those determined from CBMC simulations.

The CBMC simulations for $f_t = 1$ MPa, and varying mole fractions of $CO_2(1)$ in the bulk gas phase, y_1, are shown in Fig. 2c. The CBMC simulations show that the adsorption selectivity decreases with increasing proportion of $CO_2(1)$ in the bulk gas phase; see Fig. 2d. On the other hand, the IAST anticipates S_{ads} to increase with increasing y_1. This trend is the same as that witnessed for the experimental data for $CO_2(1)/C_3H_8(2)$ mixture adsorption in NaX zeolite; see Fig. 1d.

The failure of the IAST to provide quantitatively accurate estimates of component loadings, and adsorption selectivities is attributable to the inhomogeneous distribution of adsorbates in the pore space of NaX zeolite, caused by strong binding of CO_2 with the extra-framework cations. The inhomogeneous distribution is clearly visualized in the computational snapshot in Fig. 3 for $f_1 = 0.45$ MPa, and $f_2 = 0.55$ MPa. We note that the top left cage contains only CO_2, and there is no C_3H_8 present in that cage. One of the key assumptions of the IAST is that the distribution of adsorbates within the pore space is homogenous; this assumption is violated causing the quantitative failure of the IAST.

Since the root cause of the failure of the IAST is the inhomogeneous distribution of adsorbates engendered by strong binding of CO_2 with the extra-framework cations, we should expect the non-ideality effects to be negligibly small in all-silica zeolites, with no extra-framework cations. In order to verify this, we performed CBMC simulations $CO_2(1)/C_3H_8(2)$ mixture adsorption in all-silica FAU zeolite, with Si/Al $\rightarrow \infty$, at 300 K and total fugacity $f_t = 1$ MPa, with varying CO_2 in the

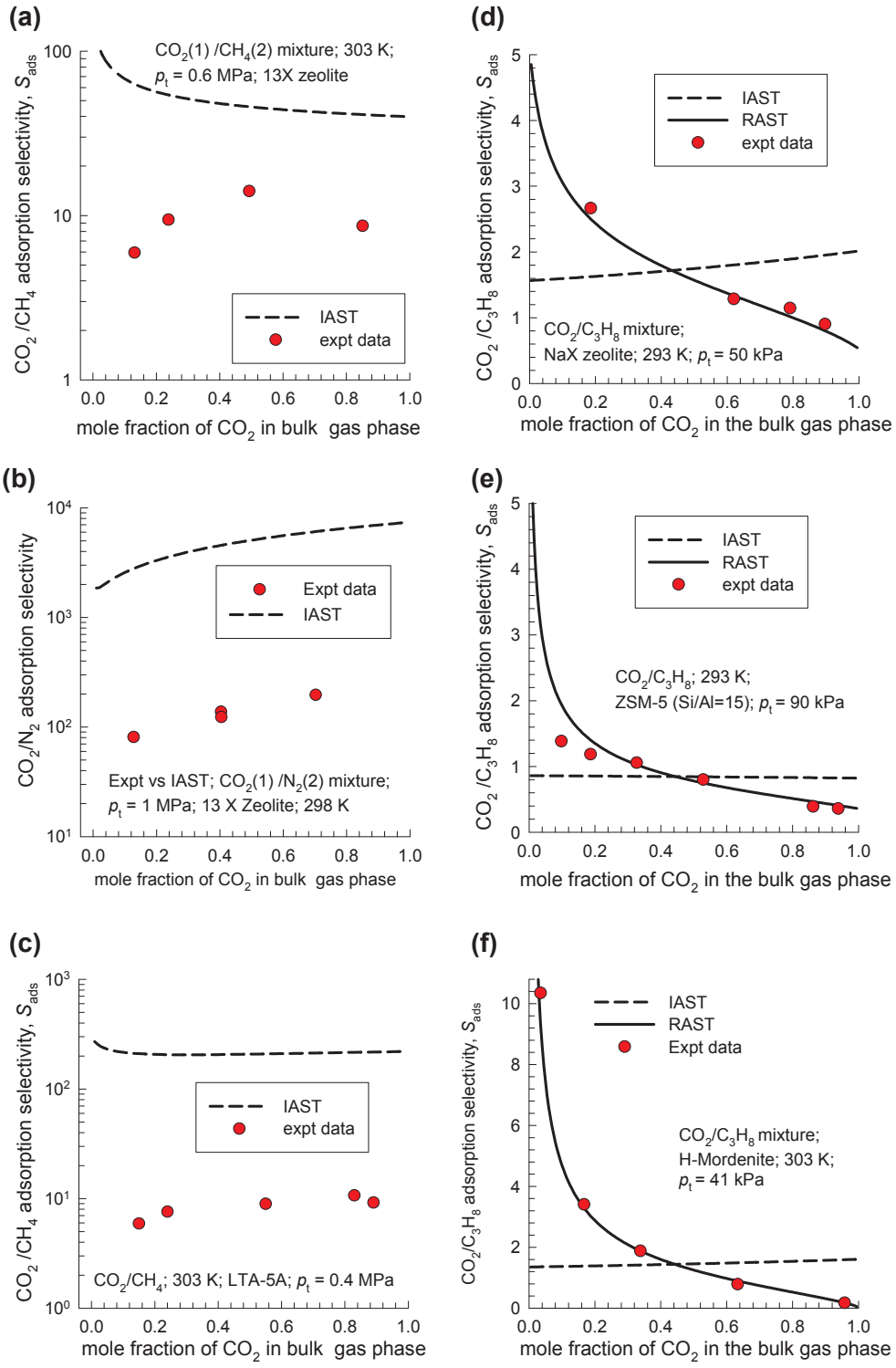

Fig. 1. Comparison of experimental data on mixture adsorption selectivity with IAST estimates for (a) CO_2/CH_4 in 13X zeolite at $T = 298$ K and $p_t = 1$ MPa [10], (b) CO_2/N_2 in 13X zeolite at $T = 298$ K and $p_t = 1$ MPa [11], (c) CO_2/CH_4 in LTA-5A zeolite at $T = 303$ K and $p_t = 0.4$ MPa [12], (d) CO_2/C_3H_8 in 13X zeolite at $T = 293$ K and $p_t = 50$ kPa [40], (e) CO_2/C_3H_8 in ZSM-5 (Si/Al = 15) at $T = 293$ K and $p_t = 90$ kPa [41], and (f) CO_2/C_3H_8 in H-MOR (= H-Mordenite) at $T = 303$ K and $p_t = 41$ kPa and [29]. In all cases, the x-axis represents the mole fraction of CO_2 in the bulk gas phase, maintained at constant total pressure, p_t, and temperature, T. All data inputs and computational details are provided in the Supplementary Material.

bulk gas phase; the results are presented in Fig. 4a. As anticipated, the IAST estimates of component loadings, and adsorption selectivities are in good agreement with CBMC data. Similar good agreement is also obtained for $CO_2(1)/C_2H_6(2)$ mixture adsorption in all-silica FAU zeolite; see Fig. 4b.

From the data in Figs. 2 and 4, we must conclude that the accuracy of IAST estimates should also depend on the Si/Al ratio of cation-exchanged zeolites. To test this hypothesis Fig. 5 presents a comparison of CO_2/CH_4 adsorption selectivities determined from CBMC simulations at 300 K for all-silica FAU (Si/Al = ∞ with 192 Si, 0 Al, 0 Na^+ per unit

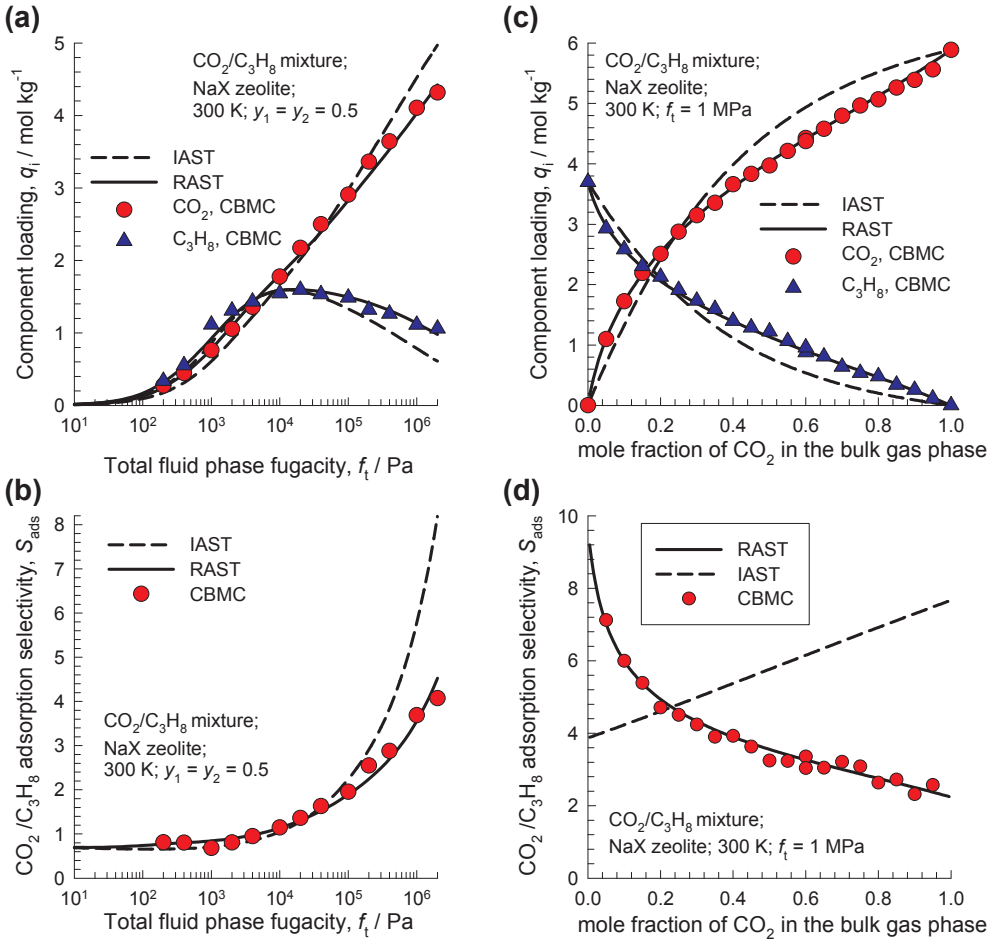

Fig. 2. (a, c) CBMC simulations (symbols) of the component loadings for $CO_2(1)/C_3H_8(2)$ mixture adsorption in NaX zeolite at 300 K. (b, d) CBMC simulations (symbols) of the $CO_2(1)/C_3H_8(2)$ adsorption selectivity. In (a, b), the *x*-axis is the total fugacity f_t in the bulk gas phase; the mole fraction of $CO_2(1)$ in the bulk gas phase is held constant, $y_1 = 0.5$. In (c, d), The IAST and RAST estimates are indicated by dashed and continuous solid lines, respectively. All data inputs and computational details are provided in the Supplementary Material.

cell), NaY (Si/Al = 2.56 with 138 Si, 54 Al, 54 Na^+ per unit cell), and NaX (Si/Al = 1.23 with 106 Si, 86 Al, 86 Na^+ per unit cell) zeolites with IAST estimations. For all-silica FAU, the IAST estimates are in perfect agreement with CBMC simulations. The agreement of IAST estimates with CBMC simulated data becomes progressively worse with decreasing Si/Al ratios. This trend confirms our contention that the failure of IAST is due to the strong interactions of CO_2 with extra-framework cations.

3. CBMC simulations of mixture adsorption in cation-exchanged LTA zeolite

We now investigate the accuracy of IAST estimates of $CO_2(1)/C_3H_8(2)$ mixture adsorption in LTA-4A zeolite, that consists of cages of 743 $Å^3$ volume, separated by 4.11 Å × 4.47 Å 8-ring windows. Per unit cell LTA-4A has 96 Si, 96 Al, 96 Na^+, with Si/Al = 1. In the CBMC simulations of $CO_2(1)/C_3H_8(2)$ mixture adsorption the mole fraction of $CO_2(1)$ in the bulk gas phase, y_1 was varied from 0 to 1, keeping the bulk gas phase mixture fugacity $f_t = f_1 + f_2$ constant at a value of 1 MPa; the results are summarized in Fig. 6a. The CBMC simulations show that the adsorption selectivity decreases with increasing proportion of $CO_2(1)$ in the bulk gas phase; see Fig. 6b. On the other hand, the IAST anticipates S_{ads} to be practically independent of y_1; this trend is similar to that witnessed in Fig. 1 e,f for the experimental data for $CO_2(1)/C_3H_8(2)$ mixture adsorption in ZSM-5 (Si/Al = 15), and H-MOR.

Fig. 7 shows computational snapshots of the location of $CO_2(1)$, and $C_3H_8(2)$ molecules within the pore topology of LTA-4A zeolite. We note that the CO_2 is almost exclusively located at the windows, or near the window entrance regions. Due to configurational restraints C_3H_8 can only located at the cage interiors. Consequently, the competition between the adsorption of CO_2 and C_3H_8 is less severe than assumed in the homogenous distribution that is inherent in the IAST prescription. The preferential perching of CO_2 at the window sites also manifests for other cage-window structures such as DDR, ERI, and CHA [23,37,38].

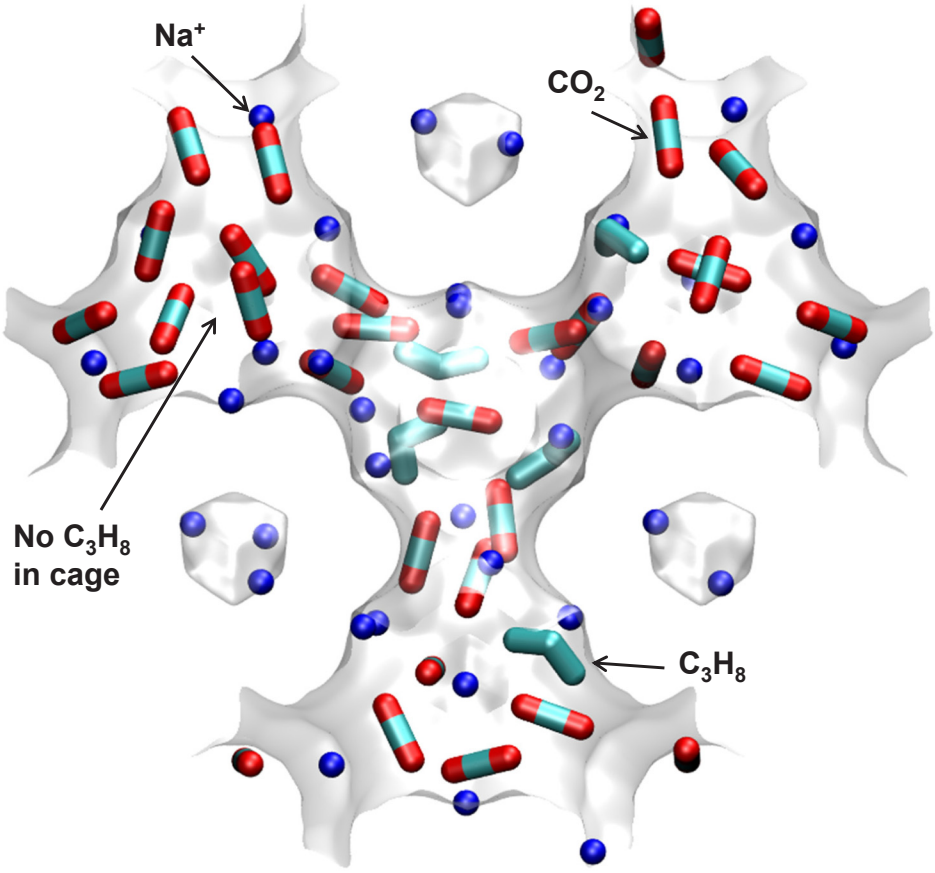

Fig. 3. Computational snapshots showing the location of CO_2, and C_3H_8 within the cages of NaX zeolite at 300 K and total fugacity f_t = 1 MPa. The component partial fugacities are f_1 = 0.45 MPa, and f_2 = 0.55 MPa.

4. Modelling non-ideal mixture adsorption using the RAST

For quantifying the departures of the IAST from CBMC data, we use the Real Adsorbed Solution Theory (RAST) [21,23,27–29,39], in which the partial fugacity of any component in the bulk fluid phase is related to the mole fraction x_i in the adsorbed phase by introduction of activity coefficients describing non-idealities in the adsorbed phase

$$f_i = P_i^0 x_i \gamma_i \tag{2}$$

From the CBMC data on $CO_2(1)/C_3H_8(2)$ mixture adsorption data in Fig. 2. the quantities $f_i/P_i^0 x_{i,CBMC}$ may be determined; these are plotted in Fig. 8a,b as function of (a) the mole fraction of CO_2 in the adsorbed phase, $x_{1,\mathrm{CBMC}}$, and (b) the adsorption potential, $\frac{\pi A}{RT}$. The plots show that appropriate models for the activity coefficient must also include the dependence on the adsorption potential [21,23,27–29,39]. The Wilson model, for example, may be written as

$$\begin{aligned}\ln(\gamma_1) &= \left(1-\ln(x_1 + x_2\Lambda_{12}) - \frac{x_1}{x_1 + x_2\Lambda_{12}} - \frac{x_2\Lambda_{21}}{x_2 + x_1\Lambda_{21}}\right)\left(1-\exp\left(-C\frac{\pi A}{RT}\right)\right)\\ \ln(\gamma_2) &= \left(1-\ln(x_2 + x_1\Lambda_{21}) - \frac{x_2}{x_2 + x_1\Lambda_{21}} - \frac{x_1\Lambda_{12}}{x_1 + x_2\Lambda_{12}}\right)\left(1-\exp\left(-C\frac{\pi A}{RT}\right)\right)\end{aligned} \tag{3}$$

In Eq. (3), C is a constant with the units kg mol^{-1}. The introduction of $\left(1-\exp\left(-C\frac{\pi A}{RT}\right)\right)$ imparts the correct limiting behaviors $\gamma_i \to 1$; $f_i \to 0$ for the activity coefficients in the Henry regime. As pore saturation conditions are approached, this correction factor tends to unity, $\left(1-\exp\left(-C\frac{\pi A}{RT}\right)\right) \to 1$. The total mixture loading is given by

$$q_t \equiv q_1 + q_2 = \frac{1}{\frac{x_1}{q_1^0(P_1^0)} + \frac{x_2}{q_2^0(P_2^0)} + [-x_1\ln(x_1 + x_2\Lambda_{12}) - x_2\ln(x_2 + x_1\Lambda_{21})]C\exp\left(-C\frac{\pi A}{RT}\right)} \tag{4}$$

The set of Eqs. (1), (2), (3), and (4) must be solved simultaneously to obtain the values of the component loadings q_1, and q_2, for a specified set of values of f_1, and f_2.

The continuous solid lines in Figs. 1, 2, and 6 represent RAST calculations in which the parameters in the Wilson model are obtained by fitting to match CBMC or experimental data on component loadings.

As illustration of the influence of thermodynamic non-idealities on the separation performance in fixed beds, let us consider CO_2/C_3H_8 separations in an adsorber packed with NaX zeolite operating at 300 K. Using the theory of shock waves for separations in fixed bed adsorbers [8,19], the maximum amount of pure C_3H_8 that can be recovered during the adsorption cycle is given by the separation potential, $\Delta Q = Q_{CO2}\frac{y_{C3H8}}{1-y_{C3H8}} - Q_{C3H8}$, expressed in the units mol per L of adsorbent; for these calculations the crystal framework density of NaX zeolite is taken as ρ = 1421 kg m^{-3}. Fig. 9. presents a comparison of the

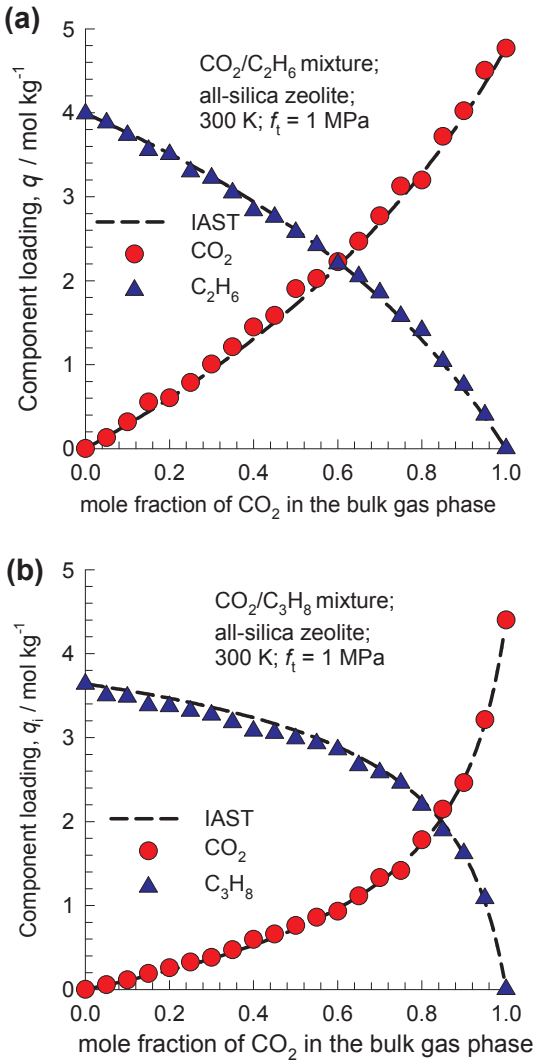

Fig. 4. CBMC simulations (symbols) of the component loadings for adsorption of (a) $CO_2(1)/C_3H_8(2)$, and (b) $CO_2(1)/C_2H_6(2)$ mixtures in all-silica FAU zeolite at 300 K and total fugacity f_t = 1 MPa. The x-axis represents the mole fraction of CO_2 in the bulk gas phase. The dashed line represent IAST estimates. All data inputs and computational details are provided in the Supplementary Material.

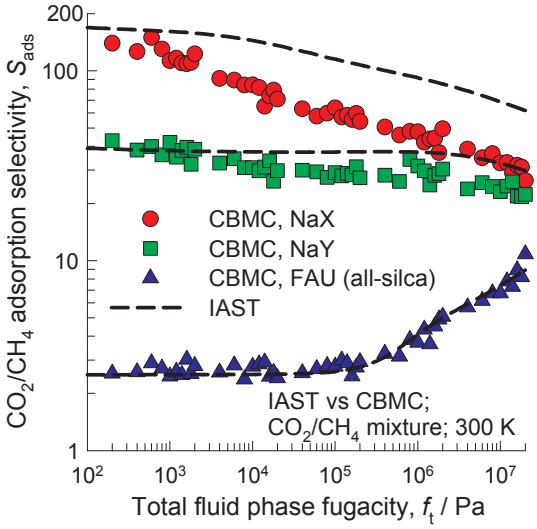

Fig. 5. Comparison CO_2/CH_4 adsorption selectivities determined from CBMC simulations 300 K for all-silica FAU (192 Si, 0 Al, 0 Na^+, Si/Al = ∞), NaY (138 Si, 54 Al, 54 Na^+, Si/Al = 2.56), and NaX (106 Si, 86 Al, 86 Na^+, Si/Al = 1.23) zeolites with IAST estimations. All data inputs and computational details are provided in the Supplementary Material.

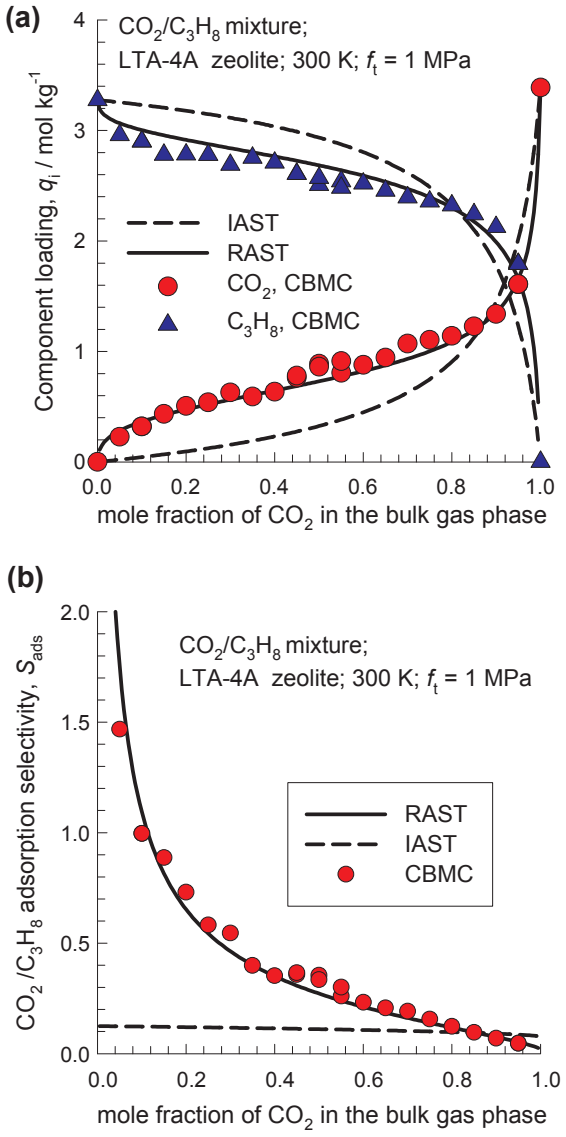

Fig. 6. (a) CBMC simulations (symbols) of the component loadings for $CO_2(1)/C_3H_8(2)$ mixture adsorption in LTA-4A zeolite at 300 K. The *x*-axis is mole fraction of CO_2 in the bulk gas phase; the total fugacity is held constant at $f_t = 1$ MPa. (b) CBMC simulations (symbols) of the $CO_2(1)/C_3H_8(2)$ adsorption selectivity. The IAST and RAST estimates are indicated by dashed and continuous solid lines, respectively. All data inputs and computational details are provided in the Supplementary Material.

IAST and RAST calculations of ΔQ; for a total mixture fugacity, $f_t = 1$ MPa, the values of ΔQ, are respectively 5.2, and 4 mol L^{-1}, respectively. Thermodynamic non-idealities reduce the productivity of pure C_3H_8 in a fixed bed adsorber by about 20%.

5. Conclusions

The following major conclusions emerge from the foregoing analysis of adsorption of CO_2-bearing mixtures in cation-exchanged zeolites. The failure of the IAST to provide quantitatively accurate estimates of mixture adsorption, as witnessed in the experimental data in Fig. 1. is ascribable to inhomogeneous distribution of adsorbates within the zeolite pores. In NaX zeolite, the inhomogeneity is a direct consequence of strong binding of CO_2 with extra-framework cations, leading congregation effects around cations. In LTA zeolites, CO_2 locates preferentially at the window regions, causing an inhomogeneous distribution of adsorbates. In the RAST description of mixture adsorption, the chosen model for activity coefficients must also include the dependence on the adsorption potential $\frac{\pi A}{RT}$.

The overall conclusion to be drawn from this study is that thermodynamic non-idealities may have a significant influence of the separations in fixed bed adsorption devices. For CO_2 capture applications with cation-exchanged zeolites, departures from idealities generally tend to reduce the separation effectiveness.

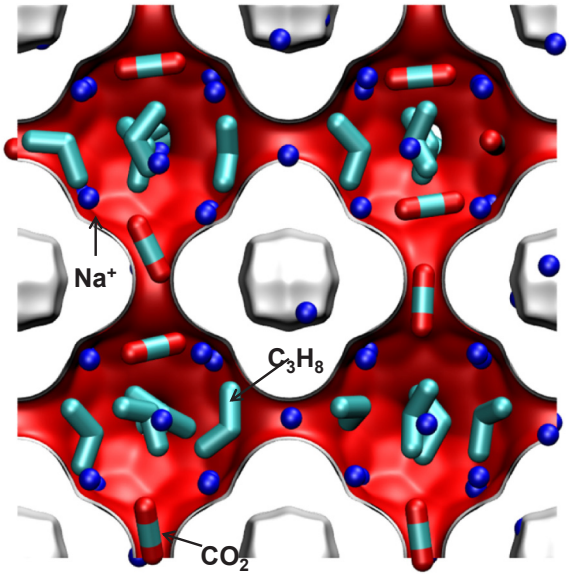

Fig. 7. Computational snapshots showing the location of CO_2, and C_3H_8 within the cages of LTA-4A zeolite at 300 K and total fugacity f_t = 1 MPa. The component partial fugacities are f_1 = 0.85 MPa, and f_2 = 0.15 MPa.

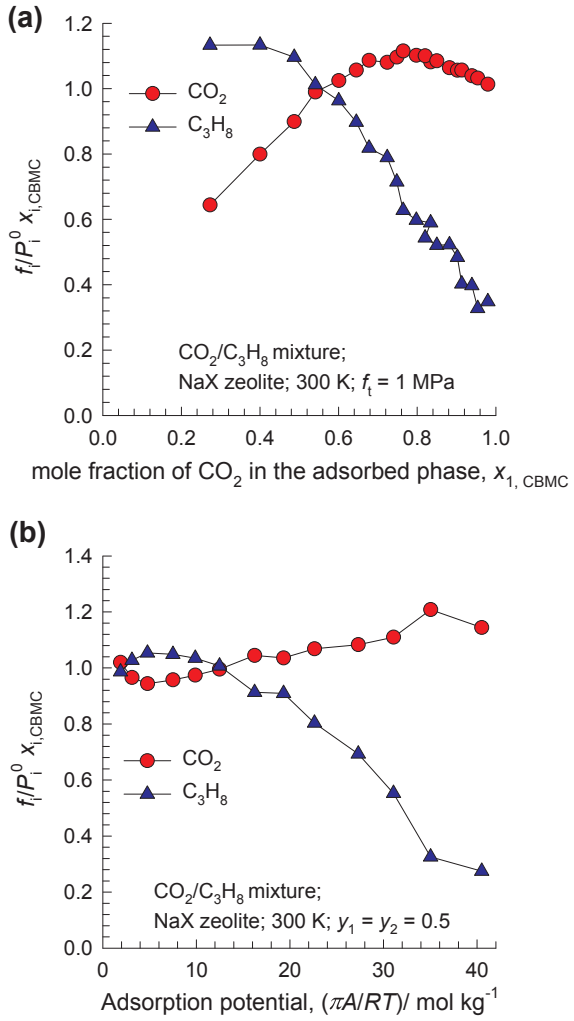

Fig. 8. Analysis of the non-idealities in $CO_2(1)/C_3H_8(2)$ mixture adsorption in NaX zeolite at 300 K. Dependence of $f_i/P_i^0 x_{i,CBMC}$ on (a) the mole fraction of CO_2 in the adsorbed phase as determined from CBMC simulations, $x_{1,CBMC}$, and (b) the adsorption potential, $\frac{\pi A}{RT}$. All data inputs and computational details are provided in the Supplementary Material.

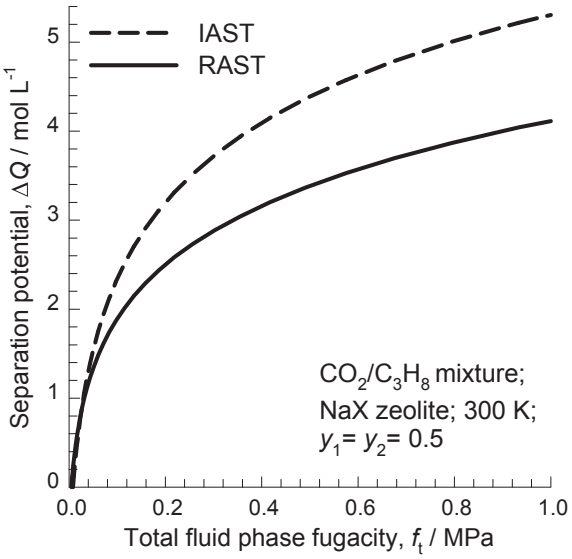

Fig. 9. Comparison of IAST and RAST calculations of the separation potential, $\Delta Q = Q_1 \frac{y_2}{y_1} - Q_2$ for separation of 50/50 $CO_2(1)/C_3H_8(2)$ feed mixtures in NaX zeolite at 300 K.

Appendix A. Supplementary material

Supplementary data associated with this article can be found, in the online version, at https://doi.org/10.1016/j.seppur.2018.06.009.

References

[1] G.D. Pirngruber, V. Carlier, D. Leinekugel-le-Cocq, Post-combustion CO_2 capture by vacuum swing adsorption using zeolites – a feasibility study, Oil Gas Sci. Technol. 69 (2014) 989–1003.

[2] J. Yang, R. Krishna, J. Li, J. Li, Experiments and simulations on separating a CO_2/CH_4 mixture using K-KFI at low and high pressures, Microporous Mesoporous Mater. 184 (2014) 21–27.

[3] M. Palomino, A. Corma, F. Rey, S. Valencia, New insights on CO_2 – methane separation using LTA zeolites with different Si/Al ratios and a first comparison with MOFs, Langmuir 26 (2010) 1910–1917.

[4] Y. Belmabkhout, G. Pirngruber, E. Jolimaitre, A. Methivier, A complete experimental approach for synthesis gas separation studies using static gravimetric and column breakthrough experiments, Adsorption 13 (2007) 341–349.

[5] R. Krishna, J.M. van Baten, In silico screening of zeolite membranes for CO_2 capture, J. Membr. Sci. 360 (2010) 323–333.

[6] R. Krishna, J.M. van Baten, In silico screening of metal-organic frameworks in separation applications, Phys. Chem. Chem. Phys. 13 (2011) 10593–10616.

[7] R. Krishna, J.M. van Baten, A comparison of the CO_2 capture characteristics of zeolites and metal-organic frameworks, Sep. Purif. Technol. 87 (2012) 120–126.

[8] R. Krishna, Methodologies for screening and selection of crystalline microporous materials in mixture separations, Sep. Purif. Technol. 194 (2018) 281–300.

[9] M.R. Hudson, L. Murray, J.A. Mason, D.W. Fickel, R.F. Lobo, W.L. Queen, C.M. Brown, Unconventional and highly selective CO_2 adsorption in zeolite SSZ-13, J. Am. Chem. Soc. 134 (2012) 1970–1973.

[10] F. Gholipour, M. Mofarahi, Adsorption equilibrium of methane and carbon dioxide on zeolite13X: experimental and thermodynamic modeling, J. Supercrit. Fluids 111 (2016) 47–54.

[11] M. Hefti, D. Marx, L. Joss, M. Mazzotti, Adsorption equilibrium of binary mixtures of carbon dioxide and nitrogen on zeolites ZSM-5 and 13X, Microporous Mesoporous Mater. 215 (2015) 215–228.

[12] M. Mofarahi, F. Gholipour, Gas adsorption separation of CO_2/CH_4 system using zeolite 5A, Microporous Mesoporous Mater. 200 (2014) 47–54.

[13] T.-H. Bae, M.R. Hudson, J.A. Mason, W.L. Queen, J.J. Dutton, K. Sumida, K.J. Micklash, S.S. Kaye, C.M. Brown, J.R. Long, Evaluation of cation-exchanged zeolite adsorbents for post-combustion carbon dioxide capture, Energy Environ. Sci. 6 (2013) 128–138.

[14] Y. Jiang, J. Ling, P. Xiao, Y. He, Q. Zhao, Z. Chu, Y. Liu, P. Li, P.A. Webley, Simultaneous biogas purification and CO_2 capture by vacuum swing adsorption using zeolite NaUSY, Chem. Eng. J. 334 (2018) 2593–2602.

[15] J. Bower, D. Barpaga, S. Prodinger, R. Krishna, H.T. Schaef, B.P. McGrail, M.A. Derewinski, R.K. Motkuri, Dynamic adsorption of CO_2/N_2 on cation-exchanged Chabazite SSZ-13: a breakthrough analysis, ACS Appl. Mater. Interfaces 10 (2018) 14287–14291.

[16] R.T. Yang, Adsorbents: Fundamentals and Applications, John Wiley & Sons Inc, Hoboken, New Jersey, 2003.

[17] J. Yang, H. Shang, R. Krishna, Y. Wang, K. Ouyang, J. Li, Adjusting the proportions of extra-framework K^+ and Cs^+ cations to construct a "molecular gate" on ZK-5 for CO_2 removal, Microporous Mesoporous Mater. 268 (2018) 50–57.

[18] D.M. Ruthven, S. Farooq, K.S. Knaebel, Pressure Swing Adsorption, VCH Publishers, New York, 1994.

[19] R. Krishna, Screening metal-organic frameworks for mixture separations in fixed-bed adsorbers using a combined selectivity/capacity metric, RSC Adv. 7 (2017) 35724–35737.

[20] R.T. Yang, Gas Separation by Adsorption Processes, Butterworth, Boston, 1987.

[21] A.L. Myers, J.M. Prausnitz, Thermodynamics of mixed gas, Adsorption 11 (A.I.Ch.E.J. 1965,) 121–130.

[22] R. Krishna, The Maxwell-Stefan description of mixture diffusion in nanoporous crystalline materials, Microporous Mesoporous Mater. 185 (2014) 30–50.

[23] R. Krishna, J.M. van Baten, R. Baur, Highlighting the origins and consequences of thermodynamic nonidealities in mixture separations using zeolites and metal-organic frameworks, Microporous Mesoporous Mater. 267 (2018) 274–292.

[24] J.A. Mason, K. Sumida, Z.R. Herm, R. Krishna, J.R. Long, Evaluating metal-organic frameworks for post-combustion carbon dioxide capture via temperature swing adsorption, Energy Environ. Sci. 4 (2011) 3030–3040.

[25] S. Divekar, A. Nanoti, S. Dasgupta, R. Aarti, P. Chauhan, M.O. Gupta, S.P. Garg, I.M. Mishra Singh, Adsorption equilibria of propylene and propane on zeolites and prediction of their binary adsorption with the ideal adsorbed solution theory, J. Chem. Eng. Data 61 (2016) 2629–2637.

[26] E. Mangano, D. Friedrich, S. Brandani, Robust algorithms for the solution of the ideal adsorbed, Solution Theory Eqs. 61 (A.I.Ch.E.J. 2015,) 981–991.

[27] F.R. Siperstein, A.L. Myers, Mixed-gas adsorption, AIChE J. 47 (2001) 1141–1159.

[28] O. Talu, A.L. Myers, Rigorous thermodynamic treatment of gas-adsorption, AIChE J. 34 (1988) 1887–1893.

[29] O. Talu, I. Zwiebel, Multicomponent adsorption equilibria of nonideal mixtures, AIChE J. 32 (1986) 1263–1276.

[30] C.-W. Wu, S. Sircar, Comments on binary and ternary gas adsorption selectivity, Sep. Purif. Technol. 170 (2016) 453–461.

[31] S.H. Hyun, R.P. Danner, Equiilbrium adsorption of ethane, ethylene, isobutane, carbon dioxide, and their binary mixtures on 13X molecular sieves, J. Chem. Eng. Data 27 (1982) 196–200.

[32] D. Frenkel, B. Smit, Understanding Molecular Simulations: From Algorithms to Applications, second ed., Academic Press, San Diego, 2002.

[33] B. Smit, R. Krishna, Molecular simulations in zeolitic process design, Chem. Eng. Sci. 58 (2003) 557–568.

[34] T.J.H. Vlugt, R. Krishna, B. Smit, Molecular simulations of adsorption isotherms for linear and branched alkanes and their mixtures in silicalite, J. Phys. Chem. B 103 (1999) 1102–1118.

[35] A. García-Sánchez, C.O. Ania, J.B. Parra, D. Dubbeldam, T.J.H. Vlugt, R. Krishna,

S. Calero, Development of a transferable force field for carbon dioxide adsorption in zeolites, J. Phys. Chem. C 113 (2009) 8814–8820.
[36] D. Dubbeldam, S. Calero, T.J.H. Vlugt, R. Krishna, T.L.M. Maesen, B. Smit, United atom forcefield for alkanes in nanoporous materials, J. Phys. Chem. B 108 (2004) 12301–12313.
[37] R. Krishna, J.M. van Baten, Segregation effects in adsorption of CO_2 containing mixtures and their consequences for separation selectivities in cage-type zeolites, Sep. Purif. Technol. 61 (2008) 414–423.
[38] R. Krishna, J.M. van Baten, Influence of segregated adsorption on mixture diffusion in DDR zeolite, Chem. Phys. Lett. 446 (2007) 344–349.
[39] J.J. Gutierrez-Sevillano, S. Calero, R. Krishna, Separation of benzene from mixtures with water, methanol, ethanol, and acetone: highlighting hydrogen bonding and molecular clustering influences in CuBTC, Phys. Chem. Chem. Phys. 17 (2015) 20114–20124.
[40] E. Costa, G. Calleja, A. Jimenez, J. Pau, Adsorption equilibrium of ethylene, propane, propylene, carbon dioxide, and their mixtures in 13X zeolite, J. Chem. Eng. Data 36 (1991) 218–224.
[41] G. Calleja, J. Pau, J.A. Calles, Pure and multicomponent adsorption equilibrium of carbon dioxide, ethylene, and propane on ZSM-5 zeolites with different Si/Al ratios, J. Chem. Eng. Data 43 (1998) 994–1003.

Supplementary Material to accompany:

Investigating the Non-idealities in Adsorption of CO_2-bearing Mixtures in Cation-exchanged Zeolites

Rajamani Krishna[a],[*] Jasper M. van Baten[b]

[a] Van 't Hoff Institute for Molecular Sciences, University of Amsterdam, Science Park 904, 1098 XH Amsterdam, The Netherlands

[b] AmsterCHEM, Almería, Spain

*email: r.krishna@contact.uva.nl

Table of Contents

1. Preamble

This Supplementary material accompanying our manuscript *Investigating the Non-idealities in Adsorption of CO_2-bearing Mixtures in Cation-exchanged Zeolites* provides:

(a) Details of the IAST, and RAST methodologies and calculations for mixture adsorption equilibria,

(b) Input data on unary isotherm fits for the wide variety of guest/host combinations examined in this article,

(c) Detailed comparisons of experimental data and CBMC data of mixture adsorption equilibrium, with IAST and RAST calculations.

(d) Wilson parameter fits for thermodynamic non-idealities

2. Summary of IAST calculation methodology

Within microporous crystalline materials, the guest molecules exist in the adsorbed phase. The Gibbs adsorption equation[1] in differential form is

$$Ad\pi = \sum_{i=1}^{n} q_i d\mu_i \qquad (1)$$

The quantity A on the left side of Equation (1) is the surface area per kg of framework, with units of m^2 per kg of the framework of the crystalline material; q_i is the molar loading of component i in the adsorbed phase with units moles per kg of framework; μ_i is the molar chemical potential of component i. The spreading pressure π has the same units as surface tension, i.e. N m^{-1}.

The chemical potential of any component in the adsorbed phase, μ_i, equals that in the bulk fluid phase. If the partial fugacities in the bulk fluid phase are f_i, we have

$$d\mu_i = RTd\ln f_i \tag{2}$$

where R is the gas constant (= 8.314 J mol^{-1} K^{-1}).

Briefly, the basic equation of Ideal Adsorbed Solution Theory (IAST) of Myers and Prausnitz[2] is the analogue of Raoult's law for vapor-liquid equilibrium, i.e.

$$f_i = P_i^0 x_i; \quad i = 1,2,...n \tag{3}$$

where x_i is the mole fraction in the adsorbed phase

$$x_i = \frac{q_i}{q_1 + q_2 + ...q_n} \tag{4}$$

and P_i^0 is the pressure for sorption of every component *i*, which yields the same spreading pressure, π for each of the pure components, as that for the mixture:

$$\frac{\pi A}{RT} = \int_0^{P_1^0} \frac{q_1^0(f)}{f} df = \int_0^{P_2^0} \frac{q_2^0(f)}{f} df = \int_0^{P_3^0} \frac{q_3^0(f)}{f} df = ... \tag{5}$$

where $q_i^0(f)$ is the *pure* component adsorption isotherm. The molar loadings $q_i^0(f)$ are expressed in the units of moles adsorbed per kg of framework, i.e. mol kg^{-1}. The units of $\frac{\pi A}{RT}$, also called the adsorption potential,[3] are mol kg^{-1}. If the isotherm fits are expressed in terms of molecules per unit cell, then the units of $\frac{\pi A}{RT}$ are also in molecules per unit cell.

The unary isotherm may be described by say the 1-site Langmuir isotherm

$$q^0(f) = q_{sat} \frac{bf}{1+bf}; \quad \theta = \frac{bf}{1+bf} \tag{6}$$

where we define the fractional *occupancy* of the adsorbate molecules, $\theta = q^0(f)/q_{sat}$. The superscript 0 is used to emphasize that $q^0(f)$ relates the *pure component* loading to the bulk fluid fugacity. More generally, the unary isotherms may need to be described by the dual-Langmuir-Freundlich model

$$q^0(f) = q_{A,sat}\frac{b_A f^{\nu A}}{1+b_A f^{\nu A}} + q_{B,sat}\frac{b_B f^{\nu B}}{1+b_B f^{\nu B}} \tag{7}$$

or the 3-site Langmuir-Freundlich model:

$$q^0 = q_{A,sat}\frac{b_A f^{\nu_A}}{1+b_A f^{\nu_A}} + q_{B,sat}\frac{b_B f^{\nu_B}}{1+b_B f^{\nu_B}} + q_{c,sat}\frac{b_C f^{\nu_C}}{1+b_C f^{\nu_C}} \tag{8}$$

Each of the integrals in Equation (5) can be evaluated analytically. For the 3-site Langmuir-Freundlich isotherm, the integration yields for component *i*,

$$\begin{aligned}
\int_{f=0}^{P_i^0}\frac{q^0(f)}{f}df &= \frac{q_{A,sat}}{\nu_A}\ln\left(1+b_A\left(P_i^0\right)^{\nu_A}\right)+\frac{q_{B,sat}}{\nu_B}\ln\left(1+b_B\left(P_i^0\right)^{\nu_B}\right)+\frac{q_{c,sat}}{\nu_C}\ln\left(1+b_C\left(P_i^0\right)^{\nu_C}\right)\\
\int_{f=0}^{P_i^0}\frac{q^0(f)}{f}df &= \frac{q_{A,sat}}{\nu_A}\ln\left(1+b_A\left(\frac{f_i}{x_i}\right)^{\nu_A}\right)+\frac{q_{B,sat}}{\nu_B}\ln\left(1+b_B\left(\frac{f_i}{x_i}\right)^{\nu_B}\right)+\frac{q_{c,sat}}{\nu_C}\ln\left(1+b_C\left(\frac{f_i}{x_i}\right)^{\nu_C}\right)
\end{aligned} \tag{9}$$

The right hand side of equation (9) is a function of P_i^0. For multicomponent mixture adsorption, each of the equalities on the right hand side of Equation (5) must satisfied. For specified partial fugacities in the bulk fluid phase, f_i, these constraints may be solved using a suitable root-finder, to yield the set of values of the adsorbed phase mole fractions, x_i, and P_i^0, all of which must satisfy Equation (5). The corresponding values of the integrals using these as upper limits of integration must yield the same value of $\frac{\pi A}{RT}$ for each component; this ensures that the obtained solution is the correct one.

A key assumption of the IAST is that the enthalpies and surface areas of the adsorbed molecules do not change upon mixing. If the total mixture loading is q_t, the area covered by the adsorbed mixture is $\frac{A}{q_t}$ with units of m^2 (mol mixture)$^{-1}$. Therefore, the assumption of no surface area change due to mixture adsorption translates as $\frac{A}{q_t} = \frac{Ax_1}{q_1^0\left(P_1^0\right)} + \frac{Ax_2}{q_2^0\left(P_2^0\right)} + \cdots \frac{Ax_n}{q_n^0\left(P_n^0\right)}$; the total mixture loading is q_t is calculated from

$$q_t \equiv q_1 + q_2 ... + q_n = \frac{1}{\frac{x_1}{q_1^0(P_1^0)} + \frac{x_2}{q_2^0(P_2^0)} + ... + \frac{x_n}{q_n^0(P_n^0)}} \tag{10}$$

in which $q_1^0(P_1^0)$, $q_2^0(P_2^0)$,… $q_n^0(P_n^0)$ are determined from the unary isotherm fits, using the sorption pressures for each component P_1^0, P_2^0, P_3^0,.. P_n^0 that are available from the solutions to equations (9), and (10).

The set of equations (3), (4), (5), (7), (8), (9), and (10) need to be solved numerically to obtain the loadings, q_i of the individual components in the mixture.

3. Activity coefficients and the Real Adsorbed Solution Theory (RAST)

To account for non-ideality effects in mixture adsorption, we introduce activity coefficients γ_i into Equation (3)[2]

$$f_i = P_i^0 x_i \gamma_i \tag{11}$$

Following the approaches of Myers, Talu, and Sieperstein[3-5] we model the excess Gibbs free energy for binary mixture adsorption as follows

$$\frac{G^{excess}}{RT} = x_1 \ln(\gamma_1) + x_2 \ln(\gamma_2) \tag{12}$$

The Wilson model for activity coefficients are given for binary mixtures by

$$\begin{aligned} \ln(\gamma_1) &= \left(1 - \ln(x_1\Lambda_{11} + x_2\Lambda_{12}) - \frac{x_1\Lambda_{11}}{x_1\Lambda_{11} + x_2\Lambda_{12}} - \frac{x_2\Lambda_{21}}{x_2 + x_1\Lambda_{21}}\right)\left(1 - \exp\left(-C\frac{\pi A}{RT}\right)\right) \\ \ln(\gamma_2) &= \left(1 - \ln(x_1\Lambda_{21} + x_2\Lambda_{22}) - \frac{x_1\Lambda_{12}}{x_1\Lambda_{11} + x_2\Lambda_{12}} - \frac{x_2\Lambda_{22}}{x_1\Lambda_{21} + x_2\Lambda_{22}}\right)\left(1 - \exp\left(-C\frac{\pi A}{RT}\right)\right) \end{aligned} \tag{13}$$

In equation (13), $\Lambda_{11} \equiv 1;\ \ \Lambda_{22} \equiv 1$, and C is a constant with the units kg mol^{-1}. The introduction of $\left(1 - \exp\left(-C\frac{\pi A}{RT}\right)\right)$ imparts the correct limiting behaviors $\gamma_i \to 1;\ \ \frac{\pi A}{RT} \to 0$ for the activity coefficients in the Henry regime, $f_t \to 0;\ \ \frac{\pi A}{RT} \to 0$. As pore saturation conditions are approached, this correction factor tends to unity $\left(1 - \exp\left(-C\frac{\pi A}{RT}\right)\right) \to 1$.

The choice of $\Lambda_{12} = \Lambda_{21} = 1$ in Equation (13) yields unity values for the activity coefficients.

The excess reciprocal loading for the mixture can be defined as

$$\left(\frac{1}{q_t}\right)^{excess} = \frac{1}{q_t} - \left(\frac{x_1}{q_1^0(P_1^0)} + \frac{x_2}{q_2^0(P_2^0)}\right) \tag{14}$$

The excess reciprocal loading for the mixture can be related to the partial derivative of the Gibbs free energy with respect to the adsorption potential at constant composition

$$\left(\frac{1}{q_t}\right)^{excess} = \left.\frac{\partial\left(\frac{G^{excess}}{RT}\right)}{\partial\left(\frac{\pi A}{RT}\right)}\right|_{T,x} = \left[-x_1 \ln(x_1 + x_2\Lambda_{12}) - x_2 \ln(x_2 + x_1\Lambda_{21})\right] C \exp\left(-C\frac{\pi A}{RT}\right) \tag{15}$$

For calculation of the total mixture loading we need to replace Equation (10) by

$$q_t \equiv q_1 + q_2 = \frac{1}{\frac{x_1}{q_1^0(P_1^0)} + \frac{x_2}{q_2^0(P_2^0)} + \left[-x_1 \ln(x_1 + x_2\Lambda_{12}) - x_2 \ln\left(x_2 + x_1\Lambda_{21}\right)\right] C \exp\left(-C\frac{\pi A}{RT}\right)} \quad (16)$$

The parameters Λ_{12}, Λ_{21}, and C can be fitted to match the experimental data on mixture adsorption or CBMC mixture simulations. The implementation of the activity coefficients is termed as the Real Adsorbed Solution Theory (RAST). For all the mixtures investigated in this article, the reported parameters Λ_{12}, Λ_{21}, and C are obtained by using the Excel solver to minimize the sum of deviations of each of the component loadings predicted by the RAST and the CBMC (or experimental) data.

A different approach to introduce the correction factor $\left(1-\exp\left(-C\frac{\pi A}{RT}\right)\right)$ into the Wilson equations has been adopted by Hefti et al.[6] for developing a RAST description of adsorption equilibrium for CO_2/N_2 mixtures in ZSM-5 and 13X zeolites for a variety of pressures ranging to 1 MPa. In their approach the Wilson coefficients Λ_{12}, and Λ_{21} are each corrected as follows

$$\Lambda_{ij} = \left(\Lambda_{ij}^0 - 1\right)\left(1-\exp\left(-C\frac{\pi A}{RT}\right)\right) + 1 \quad (17)$$

Use of the modified Wilson parameters as defined in equation (17) ensures the correct limiting behaviors $\gamma_i \to 1$; $\frac{\pi A}{RT} \to 0$ for the activity coefficients.

4. CO_2/CH_4 mixture adsorption in 13X zeolite; Re-analysis of Gholipour-Mofarahi experimental data

Gholipour and Mofarahi[7] report the results of a comprehensive experimental investigation of adsorption equilibrium of describe CO_2/CH_4 mixture adsorption in 13X zeolite at pressures of 0.4 MPa and 0.6 MPa, and varying compositions of the bulk gas mixture. We present a re-analysis of their binary experimental data at 303 K as presented in their Table 4. Figure 1a presents a plot of the adsorbed phase mole fraction of CO_2 as a function of the mole fraction of CO_2 in the bulk gas mixture; the plotted data is for 0.6 MPa total pressure. The corresponding values of the CO_2/CH_4 adsorption selectivity are plotted in Figure 1b. As compared to the experimental data, the IAST severely overpredicts the selectivity values to a significant extent.

5. CO_2/N_2 mixture adsorption in 13X zeolite; Re-analysis of Hefti experimental data

Hefti et al.[6] report the results of a comprehensive experimental investigation of adsorption equilibrium for CO_2/N_2 mixtures in ZSM-5 and 13X zeolites for pressures ranging to 1 MPa. As illustration, Figures 2a,b present experimental data (indicated by symbols) of Hefti et al.[6] for (a) component loadings, q_i, and (b) adsorbed phase mole fractions, x_i, of CO_2, and N_2 for adsorption of CO_2/N_2 mixtures in 13X zeolite at 298 K and total pressure p_t = 1 MPa, as function of the mole fraction of CO_2 in the bulk gas phase. The IAST (shown by the dashed lines) overestimates the CO_2 loading, and underestimates the N_2 loading; consequently the adsorption selectivities (see Figure 2c) are overly optimistic.

The overestimation of selectivities by IAST can be rationalized on the same basis as for CO_2/CH_4 separations with NaX zeolite, as discussed in the foregoing section. Due to strong coulombic interactions of CO_2 with the extra-framework Na^+ ions, the selectivity is strongly in favor of CO_2 There is a tendency of CO_2 molecules to congregate around the cations; as

evidenced by the snapshot in Figure 8; this results in an inhomogeneous distribution of adsorbates CO_2 and N_2. The IAST calculation assumes that N_2 molecules compete with *all* of the CO_2, making no allowance for congregation of CO_2 around the cations. Due to congregation effects, the competition faced by N_2 molecules within the cages is *smaller* than that in the entire pore space. The IAST anticipates a stiffer competition between CO_2 and N_2 as it assumes a uniform distribution of composition; consequently, the separation selectivity is *over*estimated.

Use of the RAST model, shown by the continuous solid line, with fitted Wilson parameters Λ_{12} = 1.95; Λ_{21} = 64; C = 0.044 kg mol^{-1} in Equation (13), is able to model the congregation/segregation effects in mixture adsorption. The fitted Wilson parameters are based on the entire data set at 298 K, as reported in Section 2.2 of the Supplementary Material of Hefti et al.[6] It is worthy of note here, that the RAST model calculations as presented by Hefti et al.[6] use modified Wilson parameters, described by equation (17).

6. CO_2/CH_4 mixture adsorption in LTA-5A zeolite; Re-analysis of Mofarahi-Gholipour experimental data

Mofarahi and Gholipour[8] report the results of a comprehensive experimental investigation of adsorption equilibrium of describe CO_2/CH_4 mixture adsorption in LTA-5A zeolite at 303 K, 0.4 MPa, and varying compositions of the bulk gas mixture. We present a re-analysis of their binary experimental data as presented in their Table 4, Table 9, and Table 11. Figure 3a presents a plot of the adsorbed phase mole fraction of CO_2 as a function of the mole fraction of CO_2 in the bulk gas mixture; the plotted data is for 0.4 MPa total pressure. As compared to the experimental data, the IAST severely overpredicts the mole fraction of the adsorbed phase mole fraction of CO_2. The corresponding values of the CO_2/CH_4 adsorption selectivity are plotted in Figure 3b.

As compared to the experimental data, the IAST severely overpredicts the selectivity values to a significant extent.

7. CO_2/C_3H_8 mixture adsorption in NaX zeolite; re-analysis of Costa data

Costa et al.[9] report experimental data for adsorption of $CO_2(1)/C_3H_8(2)$ mixtures in NaX zeolite at 293 K, that are analogous to those analyzed in the foregoing section for the experimental data of Siperstein and Myers[3]. The re-analysis of the data of Costa et al.[9] is presented below.

Figure 4a presents a plot of the mole fraction of CO_2 in the bulk gas phase, y_1, versus the mole fraction of CO_2 in the adsorbed phase, x_1. The experimental data clearly demonstrates the occurrence of the phenomenon of azeotropic adsorption, i.e. $y_1 = x_1$. The phenomenon of azeotropy is not anticipated by the IAST; as demonstrated the IAST calculations of x_1 versus y_1 for a total pressure of 50 kPa; see Figure 4b. Introduction of the activity coefficients in the adsorbed phase is required for quantitative modeling of mixture adsorption. The deviations from ideality are adequately described with the Wilson parameters listed in Table 3. The RAST model, with Wilson parameters fitted to match the experimental data, anticipates the phenomenon of azeotropy for bulk vapor phase mole fraction $y_1 \approx 0.8$, at a total pressure of 50 kPa; see Figure 4b.

Figure 4c presents the RAST calculations of the activity coefficients of CO_2, and C_3H_8 plotted as a function of the adsorbed phase mole fraction of CO_2, determined experimentally. It is particularly noteworthy, that the activity coefficient of propane falls significantly below unity for mole fractions of CO_2 larger than about 0.8. Figures 4d,e are parity plots, comparing the IAST and RAST estimates of the component loadings of CO_2, and C_3H_8 with the values determined

experimentally. The IAST estimates of propane loadings are seen to be in poorer agreement with experimental data. Figure 4f compares the experimentally determined CO_2/C_3H_8 selectivities with IAST and RAST estimates. Interesting, the IAST anticipates the selectivity to increase, albeit slightly with increasing y_1, whereas the experiments show a decreasing trend.

8. CO_2/C_3H_8 mixture adsorption in ZSM-5 zeolite; re-analysis of Calleja data

We present a re-analysis of the experimental data of Calleja et al.[10] for adsorption of the binary mixtures of CO_2/C_2H_4, CO_2/C_3H_8 in ZSM-5 (with MFI topology) zeolite with Si/Al ratio = 15, as reported in Table 5 of their paper.

Figure 5a presents a plot of the mole fraction of CO_2 in the bulk gas phase, y_1, versus the mole fraction of CO_2 in the adsorbed phase, x_1 for CO_2/C_3H_8 mixture The experimental data clearly demonstrates the occurrence of the phenomenon of azeotropic adsorption, i.e. $y_1 = x_1$. The phenomenon of azeotropy is not anticipated by the IAST; as demonstrated the IAST calculations of x_1 versus y_1 for a total pressure of 40 kPa; see Figure 5b. Introduction of the activity coefficients in the adsorbed phase is required for quantitative modeling of mixture adsorption. Figure 5c presents RAST calculations of the activity coefficients of CO_2, and C_3H_8 plotted as a function of the adsorbed phase mole fraction of C_2H_4, determined experimentally. Figure 5d,e are parity plots, comparing the IAST and RAST estimates of the component loadings of CO_2, and C_3H_8 with the values determined experimentally. The IAST estimates are in poorer agreement with experimental data. Figure 5f compares the experimentally determined CO_2/C_3H_8 selectivities with IAST and RAST estimates. Interesting, the IAST anticipates the selectivity to be practically independent of y_1, whereas the experiments show a decreasing trend.

9. CO_2/C_3H_8 mixture adsorption in H-MOR; re-analysis of Talu-Zwiebel data

Talu and Zwiebel[5] report experimental data of adsorption of CO_2/C_3H_8 mixtures at 303 K in H-MOR (= H-Mordenite) that provides convincing evidence of non-idealities engendered by both segregation/congregation effects; see Figures 6a,b,d,e. Two sets of experimental data are reported: (a, b) 17/83 $CO_2(1)/C_3H_8(2)$ mixtures and varying total gas phase pressures, p_t, and (d, e) $CO_2(1)/C_3H_8(2)$ mixtures at a total gas phase pressure p_t = 41 kPa, and varying CO_2 mole fractions in the bulk gas phase, y_1. The combined data set on mixture adsorption were used to determine the Wilson parameters of the RAST model; these are reported in Table 5. The corresponding RAST calculations of the activity coefficients of CO_2, and C_3H_8 for $CO_2(1)/C_3H_8(2)$ mixtures for the two data sets are shown in Figures 6c,f.

Due to congregation/segregation effects, the adsorption selectivities determined experimentally for 17/83 $CO_2(1)/C_3H_8(2)$ mixtures are significantly higher than those predicted by the IAST that assumes a uniform distribution of adsorbates within the pore topology of H-MOR; see Figures 6a,b.

The experimental data for adsorption of $CO_2(1)/C_3H_8(2)$ mixtures at a total gas phase pressure p_t = 41 kPa, and varying CO_2 mole fractions in the bulk gas phase, y_1, are presented in Figures 6d,e,f. Figure 6d compares the experimentally determined CO_2/C_3H_8 selectivities with IAST and RAST estimates for p_t = 41 kPa, and varying CO_2 mole fractions in the bulk gas phase, y_1. Interesting, the IAST anticipates the selectivity to increase, albeit slightly with increasing y_1, whereas the experiments show a decreasing trend.

The experimental data for adsorption of $CO_2(1)/C_3H_8(2)$ mixtures clearly show the phenomenon of azeotropy, at $y_1 = x_1 \approx 0.6$; see Figures 6e. The IAST does not anticipate

azeotropy. Use of the RAST model, with fitted Wilson parameters captures the azeotropic effects with good accuracy.

10. CBMC simulations for CO_2/CH_4, CO_2/N_2, and CO_2/H_2 mixture adsorption in NaX, NaY, and all-silica FAU zeolites

For CO_2 capture from natural gas, predominantly containing CH_4, at high pressures, NaX zeolite is a potential adsorbent. NaX zeolite has the Faujasite (FAU) topology and consists of cages of 786 $Å^3$ volume, separated by 7.3 Å 12-ring windows. Per unit cell of NaX zeolite we have 106 Si, 86 Al, 86 Na^+ with Si/Al=1.23. This material is also commonly referred to by its trade name: 13X zeolite.

Due to strong coulombic interactions of CO_2 with the extra-framework Na^+ ions, the selectivity is strongly in favor of CO_2. There is a tendency of CO_2 molecules to congregate around the cations; as evidenced by the snapshot in Figure 7; this results in an inhomogeneous distribution of adsorbates CO_2 and CH_4. The IAST calculation assumes that CH_4 molecules compete with *all* of the CO_2, making no allowance for congregation. Due to congregation effects, the competition faced by CH_4 molecules within the cages is *smaller* than that in the entire pore space. The IAST anticipates a stiffer competition between CO_2 and CH_4 as it assumes a uniform distribution of composition; consequently the separation selectivity is *over*estimated. This is confirmed by comparisons of the IAST estimations of CO_2/CH_4 adsorption selectivities with CBMC simulation data; see Figure 7b.

Another quantification of the departures from the IAST is to determine $f_i \left/ P_i^0 x_{i,CBMC} \right.$, where the sorption pressures P_i^0 are such that each of the equalities on the right hand side of Equation (5) are satisfied. For the IAST to hold, $f_i \left/ P_i^0 x_{i,CBMC} \right.$ should equal unity for either adsorbate.

Figure 7c shows that the $f_i \left/ P_i^0 x_{i,CBMC} \right.$ for methane falls significantly below unity, indicating that the non-ideality effects predominantly influence the component loadings of methane. Also to be concluded from Figure 7c is that the departures from ideality should also depend on the adsorption potential, $\frac{\pi A}{RT}$, that is calculated from Equation (5).

The RAST model, with activity coefficients described by the Wilson model, can be used to model congregation effects in mixture adsorption. Figure 7a compares the CBMC simulations[74, 76] for adsorption of equimolar (partial fugacities f_1=f_2) CO_2/CH_4 in NaX zeolite at 300 K with the RAST model. Congregation effects are properly modelled using the RAST. Figure 7d shows the corresponding RAST calculations of the activity coefficients γ_i, for CO_2 and CH_4. Congregation effects cause the activity coefficient of CH_4 to fall significantly below unity with increase fluid phase fugacity, f_t.

Congregation effects also manifest for adsorption of CO_2/N_2 mixtures in NaX zeolite. Figure 8a presents a comparison of CBMC simulated component loadings for 15/85 CO_2/N_2 mixture adsorption in NaX zeolite at 313 K with estimations using the IAST, and RAST. The IAST tends to overestimate the adsorption selectivities are high bulk fluid fugacities; see Figure 8b. Figure 8c presents RAST calculations of the component activity coefficients γ_i, for CO_2 and N_2; it is noteworthy that the activity coefficient of N_2 falls significantly below unity.

Figure 9 presents an analysis of 15/85 CO_2/H_2 mixture adsorption in NaX zeolite at 313 K. The deviations from IAST are also ascribable to congregation effects.

Congregation effects may be expected to become decreasingly significant as the number of extra-framework cations is reduced. To demonstrate this, Figure 10 presents a comparison CBMC CO_2/CH_4 adsorption selectivities determined from CBMC simulations at 300 K for all-silica FAU (192 Si, 0 Al, 0 Na^+, Si/Al=∞), NaY (138 Si, 54 Al, 54 Na^+, Si/Al=2.56), and NaX

(106 Si, 86 Al, 86 Na^+, Si/Al=1.23) zeolites with IAST estimations. For all-silica FAU, the IAST estimates are in perfect agreement with CBMC simulations. The agreement of IAST estimates with CBMC simulated data becomes progressively worse with decreasing Si/Al ratios.

11. CBMC simulations of CO_2/C_3H_8 mixture adsorption in NaX zeolite

The CBMC simulations of the unary isotherms for CO_2(1), and C_3H_8(2) in NaX zeolite at 300 K were fitted with the dual-Langmuir-Freundlich model; the unary isotherm fit parameters are provided in Table 6.

Two different campaigns were carried out for CBMC simulations of CO_2(1)/C_3H_8(2) mixture adsorption in NaX zeolite at 300 K:

(i) the mole fraction of CO_2(1) in the bulk gas phase is held constant, $y_1 = 0.5$, and the bulk gas phase fugacity $f_t = f_1 + f_2$ was varied, and

(ii) the mole fraction of CO_2(1) in the bulk gas phase, y_1 was varied from 0 to 1, keeping the bulk gas phase mixture fugacity $f_t = f_1 + f_2$ constant at a value of 1 MPa.

The results of these two separate campaigns are presented, respectively, in Figure 11, and Figure 12; these are discussed in turn below.

In the Henry regime of adsorption, prevailing at $f_t < 10$ kPa, the component loadings of CO_2, and C_3H_8 are nearly equal to each other (cf. Figure 11a), and the CO_2(1)/C_3H_8(2) adsorption selectivity, S_{ads}, is close to unity (cf. Figure 11b). With increasing values of the bulk gas phase fugacity f_t, above about 100 kPa, the adsorption becomes increasingly in favor of CO_2, due to strong Coulombic interactions with the extra-framework cations Na^+. The IAST estimates for the adsorption selectivity are plotted as dashed lines in Figure 11b. At $f_t = 1$ MPa, the value of $S_{ads} \approx 4$; the IAST estimate is a factor two higher than those determined from CBMC simulations.

Another quantification of the departures from the IAST is to determine $f_i \,/ P_i^0 x_{i,CBMC}$, where the sorption pressures P_i^0 are such that each of the equalities on the right hand side of Equation (5) are satisfied. For the IAST to hold, $f_i \,/ P_i^0 x_{i,CBMC}$ should equal unity for either adsorbate. Figure 11c shows that the $f_i \,/ P_i^0 x_{i,CBMC}$ for both components deviate from unity, and the deviations increase with increasing adsorption potential, $\frac{\pi A}{RT}$, that is calculated from Equation (5).

The CBMC simulations for f_t = 1 MPa, and varying mole fractions of CO_2(1) in the bulk gas phase, y_1, are shown in Figure 12. The CBMC simulations show that the adsorption selectivity decreases with increasing proportion of CO_2(1) in the bulk gas phase; see Figure 12c. On the other hand, the IAST anticipates S_{ads} to increase with increasing y_1. This trend is the same as that witnessed for the experimental data for CO_2(1)/C_3H_8(2) mixture adsorption in NaX zeolite; see Figure 4f.

Figure 12d plots $f_i \,/ P_i^0 x_{i,CBMC}$ as function of the mole fraction of CO_2 in the adsorbed phase, $x_{1,CBMC}$; For both components deviate from unity, and are composition dependent.

The failure of the IAST to provide quantitatively accurate estimates of component loadings, and adsorption selectivities is attributable to the inhomogeneous distribution of adsorbates in the pore space of NaX zeolite, caused by strong binding of CO_2 with the extra-framework cations. The inhomogeneous distribution is clearly visualized in a set of four computational snapshots

Figure 13 for f_1 = 0.05 MPa, and f_2 = 0.95 MPa.

Figure 14 for f_1 = 0.45 MPa, and f_2 = 0.55 MPa.

Figure 15 for f_1 = 0.5 MPa, and f_2 = 0.5 MPa.

Figure 16 for f_1 = 0.75 MPa, and f_2 = 0.25 MPa.

For example in Figure 14, we note that the top left cage contains only CO_2, and there is no C_3H_8 present in that cage. One of the key assumptions of the IAST is that the distribution of adsorbates within the pore space is homogenous.

For quantifying the departures from the ideal adsorbed solution theory, we use the RAST and introduce activity coefficients. For the purposes of fitting the Wilson parameters, we use the combined set of CBMC data as presented in Figure 11, and Figure 12. The fitted Wilson parameters are provided in Table 6. The RAST calculations of the component loadings, adsorbed phase mole fractions, adsorption selectivities, and activity coefficients are also presented in Figure 11, and Figure 12.

Since the root cause of the failure of the IAST is the strong binding of CO_2 with the extra-framework cations, we should expect the non-ideality effects to be negligibly small in all-silica zeolites, with no extra-framework cations. In order to verify this, we performed CBMC simulations $CO_2(1)/C_3H_8(2)$ mixture adsorption in all-silica FAU zeolite at 300 K and total fugacity f_t = 1 MPa, with varying CO_2 in the bulk gas phase; the results are presented in Figure 17. As anticipated, the IAST estimates of component loadings, and adsorption selectivities are in good agreement with CBMC data.

Figure 18 presents the corresponding CBMC simulation data (symbols) for $CO_2(1)/C_2H_6(2)$ mixture adsorption in all-silica FAU zeolite at 300 K and total fugacity f_t = 1 MPa, as function of the mole fraction of CO_2 in the bulk gas phase. Also in this case the IAST predictions are in good agreement with CBMC simulation data.

12. CBMC simulations of CO_2/C_3H_8 mixture adsorption in LTA-4A zeolite

LTA-4A zeolite consists of cages of 743 $Å^3$ volume, separated by 4.11 Å × 4.47 Å 8-ring windows. Per unit cell LTA-4A has 96 Si, 96 Al, 96 Na^+, with Si/Al=1.

The CBMC simulations of the unary isotherms for CO_2(1), and C_3H_8(2) in LTA-4A zeolite (Si/Al=1 with 96 Si, 96 Al, 96 Na^+ per unit cell) at 300 K were fitted with the dual-Langmuir model; the unary isotherm fit parameters are provided in Table 12. In the CBMC simuations for of CO_2(1)/C_3H_8(2) mixture adsorption the mole fraction of CO_2(1) in the bulk gas phase, y_1 was varied from 0 to 1, keeping the bulk gas phase mixture fugacity $f_t = f_1 + f_2$ constant at a value of 1 MPa; the results are summarized in Figure 19.

The CBMC simulations show that the adsorption selectivity decreases with increasing proportion of CO_2(1) in the bulk gas phase; see Figure 19c. On the other hand, the IAST anticipates S_{ads} to be practically independent of y_1. This trend is essentially similar as that witnessed for the experimental data for CO_2(1)/C_3H_8(2) mixture adsorption in NaX zeolite, ZSM-5 (Si/Al=15), and H-MOR; see Figure 4f , Figure 5f , and Figure 6d.

Figure 19d plots $f_i \,/\, P_i^0 x_{i,CBMC}$ as function of the mole fraction of CO_2 in the adsorbed phase, $x_{1,CBMC}$. For both components there are significant deviations from unity, indicating strong thermodynamic non-idealities. The RAST calculations of the component loadings, adsorbed phase mole fractions, adsorption selectivities, and activity coefficients are also presented as continuous solid lines in Figure 19.

Figures 20, 21, 22, 23, and 24 show snapshots of the location of CO_2(1), and C_3H_8(2) molecules within the pore topology of LTA-4A zeolite. In all case, we note that the CO_2 is almost exclusively located at the windows, or near the window entrance regions. Due to

configurational restraints C_3H_8 can only located at the cage interiors. Consequently, the competition between the adsorption of CO_2 and C_3H_8 is less severe than assumed in the homogenous distribution that is inherent in the IAST prescription.

The preferential perching of CO_2 at the window sites also manifests for other cage-window structures such as DDR, ERI, and CHA; see earlier works.[11-13]

13. Notation

A	surface area per kg of framework, $m^2\ kg^{-1}$
b_i	Langmuir-Freundlich parameter, $Pa^{-\nu}$
C	constant used in equation (13), kg mol^{-1} or uc $molecule^{-1}$
E	energy parameter, J mol^{-1}
f_i	partial fugacity of species *i*, Pa
f_t	total fugacity of bulk fluid mixture, Pa
n	number of species in the mixture, dimensionless
p_i	partial pressure of species *i*, Pa
p_t	total system pressure, Pa
P_i^0	sorption pressure, Pa
q_i	molar loading species of species *i*, mol kg^{-1}
$q_{i,sat}$	molar loading of species *i* at saturation, mol kg^{-1}
q_t	total molar loading of mixture, mol kg^{-1}
R	gas constant, 8.314 J mol^{-1} K^{-1}
S_{ads}	adsorption selectivity, dimensionless
T	absolute temperature, K
x_i	mole fraction of species *i* in adsorbed phase, dimensionless
y_i	mole fraction of species *i* in bulk fluid mixture, dimensionless

Greek letters

γ_i	activity coefficient of component *i* in adsorbed phase, dimensionless
Λ_{ij}	Wilson parameters, dimensionless
μ_i	molar chemical potential, J mol^{-1}
ν	Freundlich exponent in unary isotherm, dimensionless

π	spreading pressure, N m^{-1}
ρ	framework density, kg m^{-3}

Subscripts

1	referring to species 1
2	referring to species 2
i,j	components in mixture
i	referring to component *i*
t	referring to total mixture
sat	referring to saturation conditions

Superscripts

0	referring to pure component loading
excess	referring to excess parameter

Table 1. Dual-site Langmuir parameters for pure components CO_2, and CH_4 at 303 K in 13X zeolite. These parameters are based on the unary isotherm data reported in Figure 2 and Figure 3 of Gholipour and Mofarahi.[7]

	Site A		Site B	
	$q_{A,sat}$ mol kg^{-1}	b_A Pa^{-1}	$q_{B,sat}$ mol kg^{-1}	b_B Pa^{-1}
CO_2	3.1	9.38×10^{-6}	2.5	4.4×10^{-4}
CH_4	6.7	7.64×10^{-7}		

Table 2. Dual-site Langmuir parameters for pure components CO_2, and CH_4 at 303 K in LTA-5A zeolite. These parameters are based on the unary isotherm data reported in Figure 2 and Figure 3 of Mofarahi and Gholipour.[8]

	Site A		Site B	
	$q_{A,sat}$ mol kg^{-1}	b_A Pa^{-1}	$q_{B,sat}$ mol kg^{-1}	b_B Pa^{-1}
CO_2	1.4	7.33×10^{-6}	2.5	7.32×10^{-4}
CH_4	3.2	1.74×10^{-6}		

Table 3. Dual-site Langmuir parameters for pure components CO_2, and C_3H_8 at 293 K in 13X (= NaX) zeolite. The fit parameters were determined by fitting the unary isotherm data presented in Table I of Costa et al.[9]

	Site A		Site B	
	$q_{A,sat}$ mol kg^{-1}	b_A Pa^{-1}	$q_{B,sat}$ mol kg^{-1}	b_B Pa^{-1}
CO_2	2.2	6.7×10^{-4}	2.5	3.47×10^{-5}
C_3H_8	2.2	7.04×10^{-4}		

Wilson non-ideality parameters for binary mixtures at 293 K in NaX zeolite. These are determined by fitting to the experimental data of Costa et al.[9] as reported in their paper.

	Λ_{12}	Λ_{21}	C / kg mol^{-1}
CO_2/C_3H_8 in NaX	2	1.8	0.2

Table 4. Dual-site Langmuir parameters for pure components CO_2, and C_3H_8 at 293 K in ZSM-5 (with MFI topology) zeolite with Si/Al ratio = 15. The fit parameters were determined by fitting the unary isotherm data presented in Table 2 of Calleja et al.[10]

	Site A		Site B	
	$q_{A,sat}$ mol kg^{-1}	b_A Pa^{-1}	$q_{B,sat}$ mol kg^{-1}	b_B Pa^{-1}
CO_2	1.35	3.32×10^{-5}	1.1	4.5×10^{-3}
C_3H_8	0.76	3.62×10^{-4}	0.9	1×10^{-2}

Wilson non-ideality parameters for binary mixtures at 293 K in ZSM-5 (with MFI topology) zeolite with Si/Al ratio = 15. These are determined by fitting to the experimental data of Calleja et al.[10] as reported in Table 5 of their paper.

	Λ_{12}	Λ_{21}	C / kg mol^{-1}
CO_2/C_3H_8 in ZSM-5 (Si/Al=15)	0.2	5.1	0.9

Table 5. Dual-site Langmuir parameters for pure components CO_2, and C_3H_8 at 303 K in H-MOR. The fit parameters were determined by fitting the unary isotherm data presented in Table 4 of Talu and Zwiebel.[5]

	Site A		Site B	
	$q_{A,sat}$ mol kg^{-1}	b_A Pa^{-1}	$q_{B,sat}$ mol kg^{-1}	b_B Pa^{-1}
CO_2	2.4	2.02×10^{-5}	0.6	1.37×10^{-3}
C_3H_8	0.65	1.63×10^{-5}	0.72	1.7×10^{-3}

Wilson non-ideality parameters for binary mixtures at 303 K in H-MOR. These are determined by fitting to the experimental data of Talu and Zwiebel[5] as reported in Table 5 of their paper.

	Λ_{12}	Λ_{21}	C / kg mol^{-1}
CO_2/C_3H_8 in H-MOR	4.15	7.25	0.7

Table 6. Dual-site Langmuir-Freundlich parameters for pure components CO_2, and C_3H_8 at 300 K in NaX zeolite containing 86 Na^+/uc with Si/Al=1.23. The fit parameters are based on the CBMC simulations of pure component isotherms.

	Site A			Site B		
	$q_{A,sat}$ mol kg^{-1}	b_A Pa$^{-\nu_A}$	ν_A dimensionless	$q_{B,sat}$ mol kg^{-1}	b_B Pa$^{-\nu_B}$	ν_B dimensionless
CO_2	2.1	1.57×10^{-4}	0.7	4.4	4.26×10^{-4}	1
C_3H_8	3.1	9.85×10^{-4}	1	0.7	6.17×10^{-6}	1

Fitted Wilson non-ideality parameters for binary CO_2/C_3H_8 mixture adsorption in NaX at 300 K.

	Λ_{12}	Λ_{21}	C / kg mol^{-1}
CO_2/C_3H_8 in NaX (86 Na/uc) at 300 K	2.05	1.2	3.2

Table 7. Dual-site Langmuir-Freundlich parameters for pure components CO_2, C_2H_6 and C_3H_8 at 300K in all-silica FAU. The fit parameters are based on the CBMC simulations of pure component isotherms.

	Site A			Site B		
	$q_{A,sat}$ mol kg^{-1}	b_A Pa$^{-\nu_A}$	ν_A dimensionless	$q_{B,sat}$ mol kg^{-1}	b_B Pa$^{-\nu_B}$	ν_B dimensionless
CO_2	2.5	9.62×10^{-15}	2.5	4.1	1.09×10^{-6}	1
C_2H_6	1.8	1.1×10^{-11}	2.1	3	2.89×10^{-6}	1
C_3H_8	1.2	2.88×10^{-15}	3.4	2.6	1.51×10^{-5}	1

Table 8. Dual-site Langmuir-Freundlich parameters for pure components CO_2, and CH_4 at 300 K in NaX zeolite containing 86 Na^+/uc with Si/Al=1.23. The fit parameters are based on the CBMC simulations of pure component isotherms.

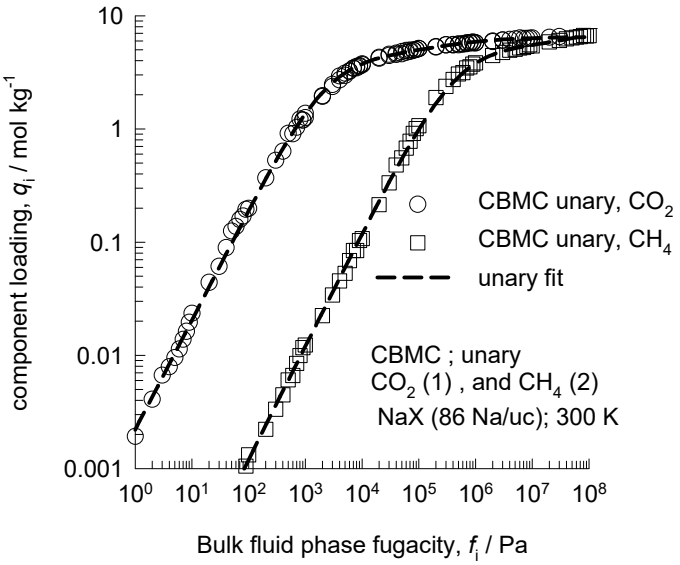

	Site A			Site B		
	$q_{A,sat}$ mol kg^{-1}	b_A Pa$^{-\nu_A}$	ν_A dimensionless	$q_{B,sat}$ mol kg^{-1}	b_B Pa$^{-\nu_B}$	ν_B dimensionless
CO_2	2.1	1.57×10^{-4}	0.7	4.4	4.26×10^{-4}	1
CH_4	2.3	1.24×10^{-8}	1	5.5	2.17×10^{-6}	1

Fitted Wilson non-ideality parameters for binary CO_2/CH_4 mixture adsorption in NaX at 300 K.

	Λ_{12}	Λ_{21}	C / kg mol^{-1}
CO_2/CH_4 in NaX (86 Na/uc) at 300 K	0.18	4.5	0.33

Table 9. Dual-site Langmuir-Freundlich parameters for pure components CO_2, N_2 and H_2 at 313 K in NaX zeolite containing 86 Na^+/uc with Si/Al=1.23. The fit parameters are based on the CBMC simulations of pure component isotherms.

	Site A			Site B		
	$q_{A,sat}$ mol kg^{-1}	b_A Pa$^{-\nu_A}$	ν_A dimensionless	$q_{B,sat}$ mol kg^{-1}	b_B Pa$^{-\nu_B}$	ν_B dimensionless
CO_2	2.25	6.64×10^{-5}	0.7	4.5	1.86×10^{-4}	1
N_2	5.6	2.85×10^{-9}	1	3.7	1.2×10^{-7}	1
H_2	9.8	4.33×10^{-10}	1	11	1.29×10^{-8}	1

Fitted Wilson non-ideality parameters for binary CO_2/N_2, and CO_2/H_2 mixture adsorption in NaX at 313 K.

	Λ_{12}	Λ_{21}	C / kg mol^{-1}
CO_2/N_2 in NaX (86 Na/uc) at 313 K	1.76	0.6	0.2
CO_2/H_2 in NaX (86 Na/uc) at 313 K	1	10^3	0.001

Table 10. Dual-site Langmuir-Freundlich parameters for pure components CO_2, and CH_4 at 300 K in NaY zeolite containing 54 Na^+/uc with Si/Al=2.56. The fit parameters are based on the CBMC simulations of pure component isotherms.

	Site A			Site B		
	$q_{A,sat}$ mol kg^{-1}	b_A Pa$^{-\nu_A}$	ν_A dimensionless	$q_{B,sat}$ mol kg^{-1}	b_B Pa$^{-\nu_B}$	ν_B dimensionless
CO_2	1.8	2×10^{-5}	0.7	5.9	4.16×10^{-5}	1
CH_4	3.4	6.53×10^{-9}	1	5.9	1.13×10^{-6}	1

Table 11. Dual-site Langmuir-Freundlich parameters for pure components CO_2, and CH_4 at 300K in all-silica FAU. The fit parameters are based on the CBMC simulations of pure component isotherms presented in earlier works.[14-16]

	Site A			Site B		
	$q_{A,sat}$ mol kg^{-1}	b_A Pa$^{-\nu_A}$	ν_A dimensionless	$q_{B,sat}$ mol kg^{-1}	b_B Pa$^{-\nu_B}$	ν_B dimensionless
CO_2	2.4	2.52×10^{-14}	2.4	6.7	6.74×10^{-7}	1
CH_4	4	7×10^{-9}	0.86	6.5	2.75×10^{-7}	1

Table 12. Dual-site Langmuir-Freundlich parameters for pure components CO_2, and C_3H_8 at 300 K in LTA-4A zeolite (96 Si, 96 Al, 96 Na^+, Si/Al=1). The fit parameters are based on the CBMC simulations of pure component isotherms.

	Site A			Site B		
	$q_{A,sat}$ mol kg^{-1}	b_A $Pa^{-\nu_A}$	ν_A dimensionless	$q_{B,sat}$ mol kg^{-1}	b_B $Pa^{-\nu_B}$	ν_B dimensionless
CO_2	3.1	4.13×10^{-4}	1	1.7	2.095×10^{-7}	1
C_3H_8	2.5	2.21×10^{-2}	1	0.9	6.18×10^{-6}	1

Fitted Wilson non-ideality parameters for binary CO_2/C_3H_8 mixture adsorption in LTA-4A at 300 K.

	Λ_{12}	Λ_{21}	C / kg mol^{-1}
CO_2/C_3H_8 in LTA-4A at 300 K	0.001	10.5	3.2

14. References

(1) Ruthven, D. M. *Principles of Adsorption and Adsorption Processes*; John Wiley: New York, 1984.

(2) Myers, A. L.; Prausnitz, J. M. Thermodynamics of Mixed Gas Adsorption. *A.I.Ch.E.J.* **1965**, *11*, 121-130.

(3) Siperstein, F. R.; Myers, A. L. Mixed-Gas Adsorption. *A.I.Ch.E.J.* **2001**, *47*, 1141-1159.

(4) Talu, O.; Myers, A. L. Rigorous Thermodynamic Treatment of Gas-Adsorption. *A.I.Ch.E.J.* **1988**, *34*, 1887-1893.

(5) Talu, O.; Zwiebel, I. Multicomponent Adsorption Equilibria of Nonideal Mixtures. *A.I.Ch.E.J.* **1986**, *32*, 1263-1276.

(6) Hefti, M.; Marx, D.; Joss, L.; Mazzotti, M. Adsorption Equilibrium of Binary Mixtures of Carbon Dioxide and Nitrogen on Zeolites ZSM-5 and 13X. *Microporous Mesoporous Mater.* **2015**, *215*, 215-228.

(7) Gholipour, F.; Mofarahi, M. Adsorption Equilibrium of Methane and Carbon Dioxide on Zeolite13X: Experimental and Thermodynamic Modeling. *J. of Supercritical Fluids* **2016**, *111*, 47-54.

(8) Mofarahi, M.; Gholipour, F. Gas Adsorption Separation of CO_2/CH_4 System using Zeolite 5A. *Microporous Mesoporous Mater.* **2014**, *200*, 47-54.

(9) Costa, E.; Calleja, G.; Jimenez, A.; Pau, J. Adsorption Equilibrium of Ethylene, Propane, Propylene, Carbon Dioxide, and Their Mixtures in 13X Zeolite. *J. Chem. Eng. Data* **1991**, *36*, 218-224.

(10) Calleja, G.; Pau, J.; Calles, J. A. Pure and Multicomponent Adsorption Equilibrium of Carbon Dioxide, Ethylene, and Propane on ZSM-5 Zeolites with Different Si/Al Ratios. *J. Chem. Eng. Data* **1998**, *43*, 994-1003.

(11) Krishna, R.; van Baten, J. M. Segregation effects in adsorption of CO_2 containing mixtures and their consequences for separation selectivities in cage-type zeolites. *Sep. Purif. Technol.* **2008**, *61*, 414-423.

(12) Krishna, R.; van Baten, J. M. Influence of segregated adsorption on mixture diffusion in DDR zeolite. *Chem. Phys. Lett.* **2007**, *446*, 344-349.

(13) Krishna, R.; van Baten, J. M.; Baur, R. Highlighting the Origins and Consequences of Thermodynamic Nonidealities in Mixture Separations using Zeolites and Metal-Organic Frameworks. *Microporous Mesoporous Mater.* **2018**, *267*, 274-292. http://dx.doi.org/10.1016/j.micromeso.2018.03.013.

(14) Krishna, R.; van Baten, J. M. Investigating cluster formation in adsorption of CO_2, CH_4, and Ar in zeolites and metal organic frameworks at sub-critical temperatures. *Langmuir* **2010**, *26*, 3981-3992.

(15) Krishna, R.; van Baten, J. M. Highlighting a variety of unusual characteristics of adsorption and diffusion in microporous materials induced by clustering of guest molecules. *Langmuir* **2010**, *26*, 8450-8463.

(16) Krishna, R.; van Baten, J. M. In silico screening of metal-organic frameworks in separation applications. *Phys. Chem. Chem. Phys.* **2011**, *13*, 10593-10616.

15. Captions for Figures

Figure 1. Re-analysis of the experimental data of Gholipour and Mofarahi[7] for $CO_2(1)/CH_4(2)$ mixture adsorption at 303 K in 13X zeolite. (a) Experimental data (indicated by symbols) of adsorbed phase mole fractions, x_1, of CO_2, as function of the mole fraction of CO_2 in the bulk gas phase. (b) $CO_2(1)/CH_4(2)$ adsorption selectivity as function of the mole fraction of CO_2 in the bulk gas phase. (c) Dependence of $f_i \left/ P_i^0 x_{i,\text{expt}} \right.$ on the mole fraction of CO_2 in the adsorbed phase as determined from experiments, $x_{1,\text{expt}}$. The dashed lines are the IAST estimations, using the unary isotherm fits, specified in Table 1.

Figure 2. (a, b) Experimental data (indicated by symbols) of Hefti et al.[6] for (a) component loadings, q_i, and (b) adsorbed phase mole fractions, x_i, of CO_2, and N_2 for adsorption of CO_2/N_2 mixtures in 13X zeolite at 298 K and total pressure p_t = 1 MPa, as function of the mole fraction of CO_2 in the bulk gas phase. (c) CO_2/N_2 adsorption selectivity as function of the mole fraction of CO_2 in the bulk gas phase. (d) Dependence of $f_i \left/ P_i^0 x_{i,\text{expt}} \right.$ on the mole fraction of CO_2 in the adsorbed phase as determined from experiments, $x_{1,\text{expt}}$. The dashed lines in (a), (b), and (c) are the IAST estimations, using the unary isotherm fits provided in Table 2 of Hefti et al.[6] The continuous solid lines in (a), (b), and (c) are the estimations using RAST using Wilson parameters: $\Lambda_{12} = 1.95$; $\Lambda_{21} = 64$; $C = 0.044$ kg mol^{-1}.

Figure 3. Re-analysis of the experimental data of Mofarahi and Gholipour[8] for $CO_2(1)/CH_4(2)$ mixture adsorption at 303 K in LTA-5A zeolite. (a) Experimental data (indicated by symbols) of adsorbed phase mole fractions, x_1, of CO_2, as function of the mole fraction of CO_2 in the bulk gas phase. (b) $CO_2(1)/CH_4(2)$ adsorption selectivity as function of the mole fraction of CO_2 in the bulk gas phase. (c) Dependence of $f_i \,/\, P_i^0 x_{i,\mathrm{expt}}$ on the mole fraction of CO_2 in the adsorbed phase as determined from experiments, $x_{1,\mathrm{expt}}$. The unary isotherm fit parameters are specified in Table 2.

Figure 4. Re-analysis of the experimental data of Costa et al.[9] for adsorption of CO_2/C_3H_8 mixtures at 293 K in NaX (=13 X) zeolite. (a) Plot of the experimental data on mole fraction of CO_2 in the bulk gas phase, y_1, versus the mole fraction of CO_2 in the adsorbed phase, x_1. (b) Comparison of IAST and RAST calculations of mole fraction of CO_2 in the adsorbed phase, x_1, as a function of the mole fraction of CO_2 in the bulk gas phase, y_1; the total pressure = 50 kPa. (c) Dependence of $f_i \,/\, P_i^0 x_{i,\mathrm{expt}}$ on the mole fraction of CO_2 in the adsorbed phase as determined from experiments, $x_{1,\mathrm{expt}}$. (d, e) Parity plots, comparing the IAST and RAST estimates of the component loadings of (d) CO_2, and (e) C_3H_8 with the values determined experimentally. (f) CO_2/C_3H_8 adsorption selectivity as a function of the mole fraction of CO_2 in the bulk gas phase, y_1. The unary isotherm fit parameters, along with the Wilson parameters, are specified in Table 3.

Figure 5. Re-analysis of the experimental data of Calleja et al.[10] for adsorption of CO_2/C_3H_8 mixtures at 293 K in ZSM-5 (with MFI topology) zeolite with Si/Al ratio = 15, as reported in Table 5 of their paper. (a) Plot of the experimental data on mole fraction of CO_2 in the bulk gas phase, y_1, versus the mole fraction of CO_2 in the adsorbed phase, x_1. (b) Comparison of IAST and RAST calculations of mole fraction of CO_2 in the adsorbed phase, x_1, as a function of the mole fraction of CO_2 in the bulk gas phase, y_1; p_t = 90 kPa. (c) Dependence of $f_i \left/ P_i^0 x_{i,\exp t} \right.$ on the mole fraction of CO_2 in the adsorbed phase as determined from experiments, $x_{1,\text{expt}}$. (d, e) Parity plots, comparing the IAST and RAST estimates of the component loadings of (d) CO_2, and (e) C_3H_8 with the values determined experimentally. (f) Dependence of CO_2/C_3H_8 adsorption selectivity on mole fraction of CO_2 in the bulk gas phase, y_1; experimental data for p_t = 90 kPa compared with IAST and RAST calculations. (f) CO_2/C_3H_8 adsorption selectivity as a function of the mole fraction of CO_2 in the bulk gas phase, y_1. The unary isotherm fit parameters, along with the Wilson parameters, are specified in Table 4.

Figure 6. Re-analysis of the experimental data of Talu and Zwiebel[5] for adsorption of CO_2/C_3H_8 mixtures at 303 K in H-MOR, as reported in Table 5 of their paper. (a) Dependence of $f_i \left/ P_i^0 x_{i,\exp t} \right.$ on the mole fraction of CO_2 in the adsorbed phase as determined from experiments, $x_{1,\text{expt}}$. (b, c) Comparison of experimental data with IAST and RAST calculations for the (b) adsorption selectivity, and (c) CO_2 uptake for 17/83 $CO_2(1)/C_3H_8(2)$ mixtures and varying total

gas phase pressures, p_t. (d, e) Comparison of experimental data for the (a) adsorption selectivity, and (b) adsorbed phase mole fraction of CO_2, x_1, for $CO_2(1)/C_3H_8(2)$ mixtures at a total gas phase pressure p_t = 41 kPa, and varying CO_2 mole fractions in the bulk gas phase, y_1. The unary isotherm fit parameters, along with the Wilson parameters, are specified in Table 5.

Figure 7. (a) Comparison of the estimations using the IAST, and RAST with CBMC simulations[16] of component loadings of equimolar (partial fugacities f_1=f_2) CO_2/CH_4 mixtures in NaX zeolite at 300 K. (b) Comparison CO_2/CH_4 adsorption selectivities obtained from CBMC with IAST and RAST estimations. (c) Dependence of $f_i \,/\, P_i^0 x_{i,CBMC}$ on the adsorption potential, $\frac{\pi A}{RT}$. (d) RAST calculations of the component activity coefficients γ_i, for CO_2 and CH_4. The unary isotherm fit parameters and Wilson parameters are provided in Table 8.

Figure 8. (a) Comparison of the estimations using the IAST, and RAST with CBMC simulations[16] of component loadings of 15/85 CO_2/N_2 mixtures in NaX zeolite at 313 K. (b) Comparison CO_2/N_2 adsorption selectivities obtained from CBMC with IAST and RAST estimations. (c) RAST calculations of the component activity coefficients γ_i, for CO_2 and N_2. The unary isotherm fit parameters and Wilson parameters are provided in Table 9.

Figure 9. (a) Comparison of the estimations using the IAST, and RAST with CBMC simulations[16] of component loadings of 15/85 CO_2/H_2 mixtures in NaX zeolite at 313 K. (b) Comparison CO_2/H_2 adsorption selectivities obtained from CBMC with IAST and RAST estimations. (c) RAST calculations of the component activity coefficients γ_i, for CO_2 and H_2. The unary isotherm fit parameters and Wilson parameters are provided in Table 9.

Figure 10. Comparison CBMC CO_2/CH_4 adsorption selectivities determined from CBMC simulations 300 K for all-silica FAU (192 Si, 0 Al, 0 Na^+, Si/Al=∞), NaY (138 Si, 54 Al, 54 Na^+, Si/Al=2.56), and NaX (106 Si, 86 Al, 86 Na^+, Si/Al=1.23) zeolites with IAST estimations. The unary isotherm parameters are provided in Table 11 (all-silica FAU), Table 10 (NaY), and Table 8 (NaX).

Figure 11. (a) CBMC simulations (symbols) of the component loadings for $CO_2(1)/C_3H_8(2)$ mixture adsorption in NaX zeolite at 300 K and, as function of the total fugacity f_t in the bulk gas phase. The mole fraction of $CO_2(1)$ in the bulk gas phase is held constant, $y_1 = 0.5$. (b) CBMC simulations (symbols) of the $CO_2(1)/C_3H_8(2)$ adsorption selectivity compared with RAST and IAST estimates. (c) Dependence of $f_i \left/ P_i^0 x_{i,CBMC} \right.$ on the adsorption potential, $\frac{\pi A}{RT}$. (d) RAST calculations of the component activity coefficients γ_i, for CO_2 and C_3H_8. The unary isotherm fit parameters and Wilson parameters are provided in Table 6.

Figure 12. (a, b) CBMC simulations (symbols) of the (a) component loadings, and (b) adsorbed phase mole fractions, x_1, of CO_2 for $CO_2(1)/C_3H_8(2)$ mixture adsorption in NaX zeolite at 300 K and total fugacity f_t = 1 MPa, as function of the mole fraction of CO_2 in the bulk gas phase. The continuous solid lines and dashed lines are RAST and IAST estimates. (c) CBMC simulations (symbols) of the $CO_2(1)/C_3H_8(2)$ adsorption selectivity compared with RAST and IAST estimates. (d) Dependence of $f_i \left/ P_i^0 x_{i,CBMC} \right.$ on the mole fraction of CO_2 in the adsorbed phase as determined from CBMC simulations, $x_{1,CBMC}$. (e) RAST calculations of the component activity coefficients γ_i, for CO_2 and C_3H_8. The unary isotherm fit parameters and Wilson parameters are provided in Table 6.

Figure 13. Computational snapshots showing the location of CO_2, and C_3H_8 within the cages of NaX zeolite at 300 K and total fugacity f_t = 1 MPa. The component partial fugacities are f_1 = 0.05 MPa, and f_2 = 0.95 MPa.

Figure 14. Computational snapshots showing the location of CO_2, and C_3H_8 within the cages of NaX zeolite at 300 K and total fugacity f_t = 1 MPa. The component partial fugacities are f_1 = 0.45 MPa, and f_2 = 0.55 MPa.

Figure 15. Computational snapshots showing the location of CO_2, and C_3H_8 within the cages of NaX zeolite at 300 K and total fugacity f_t = 1 MPa. The component partial fugacities are f_1 = 0.5 MPa, and f_2 = 0.5 MPa.

Figure 16. Computational snapshot showing the location of CO_2, and C_3H_8 within the cages of NaX zeolite at 300 K and total fugacity f_t = 1 MPa. The component partial fugacities are f_1 = 0.75 MPa, and f_2 = 0.25 MPa.

Figure 17. (a, b, c) CBMC simulations (symbols) of the (a) component loadings, (b) adsorbed phase mole fractions, x_1, of CO_2, and (c) $CO_2(1)/C_3H_8(2)$ adsorption selectivity for $CO_2(1)/C_3H_8(2)$ mixture adsorption in all-silica FAU zeolite at 300 K and total fugacity f_t = 1 MPa. The x-axis represents the mole fraction of CO_2 in the bulk gas phase. The dashed line represent IAST estimates. (d, e) Parity plots, comparing the IAST estimates of the component loadings of (d) CO_2, and (e) C_3H_8 with the values determined from CBMC simulations. The unary isotherm fit parameters are provided in Table 7.

Figure 18. (a, b, c) CBMC simulations (symbols) of the (a) component loadings, (b) adsorbed phase mole fractions, x_1, of CO_2, and (c) $CO_2(1)/C_2H_6(2)$ adsorption selectivity for $CO_2(1)/C_2H_6(2)$ mixture adsorption in all-silica FAU zeolite at 300 K and total fugacity f_t = 1 MPa. The x-axis represents the mole fraction of CO_2 in the bulk gas phase. The dashed line represent IAST estimates. (d, e) Parity plots, comparing the IAST estimates of the component

loadings of (d) CO_2, and (e) C_2H_6 with the values determined from CBMC simulations. The unary isotherm fit parameters are provided in Table 7.

Figure 19. (a, b) CBMC simulations (symbols) of the (a) component loadings, and (b) adsorbed phase mole fractions, x_1, of CO_2 for $CO_2(1)/C_3H_8(2)$ mixture adsorption in LTA-4A zeolite at 300 K and total fugacity f_t = 1 MPa, as function of the mole fraction of CO_2 in the bulk gas phase. The continuous solid lines and dashed lines are RAST and IAST estimates. (c) CBMC simulations (symbols) of the $CO_2(1)/C_3H_8(2)$ adsorption selectivity compared with RAST and IAST estimates. (d) Dependence of $f_i \,/ P_i^0 x_{i,CBMC}$ on the mole fraction of CO_2 in the adsorbed phase as determined from CBMC simulations, $x_{1,CBMC}$. (e) RAST calculations of the component activity coefficients γ_i, for CO_2 and C_3H_8. The unary isotherm fit parameters and Wilson parameters are provided in Table 12.

Figure 20. Computational snapshot showing the location of CO_2, and C_3H_8 within the cages of LTA-4A zeolite at 300 K and total fugacity f_t = 1 MPa. The component partial fugacities are f_1 = 0.25 MPa, and f_2 = 0.75 MPa.

Figure 21. Computational snapshot showing the location of CO_2, and C_3H_8 within the cages of LTA-4A zeolite at 300 K and total fugacity f_t = 1 MPa. The component partial fugacities are f_1 = 0.55 MPa, and f_2 = 0.45 MPa.

Figure 22. Computational snapshot showing the location of CO_2, and C_3H_8 within the cages of LTA-4A zeolite at 300 K and total fugacity f_t = 1 MPa. The component partial fugacities are f_1 = 0.65 MPa, and f_2 = 0.35 MPa.

Figure 23. Computational snapshot showing the location of CO_2, and C_3H_8 within the cages of LTA-4A zeolite at 300 K and total fugacity f_t = 1 MPa. The component partial fugacities are f_1 = 0.8 MPa, and f_2 = 0.2 MPa.

Figure 24. Computational snapshot showing the location of CO_2, and C_3H_8 within the cages of LTA-4A zeolite at 300 K and total fugacity f_t = 1 MPa. The component partial fugacities are f_1 = 0.85 MPa, and f_2 = 0.15 MPa.

CO_2/CH_4 mixture adsorption in 13X zeolite: Re-analysis of Gholipour-Mofarahi data

Figure S1

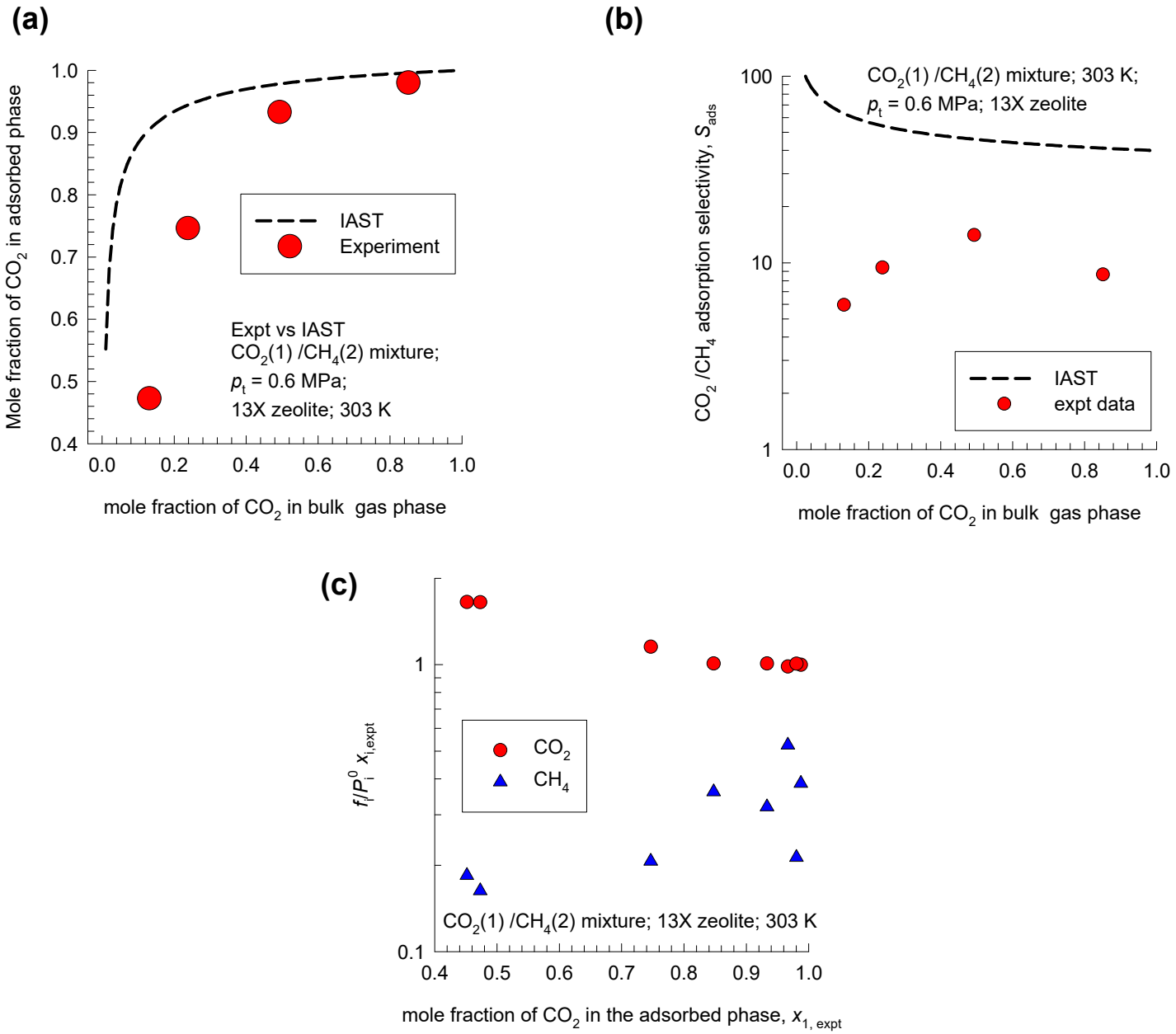

CO_2/N_2 mixture adsorption in 13X zeolite; Re-analysis of data of Hefti et al.

Figure S2

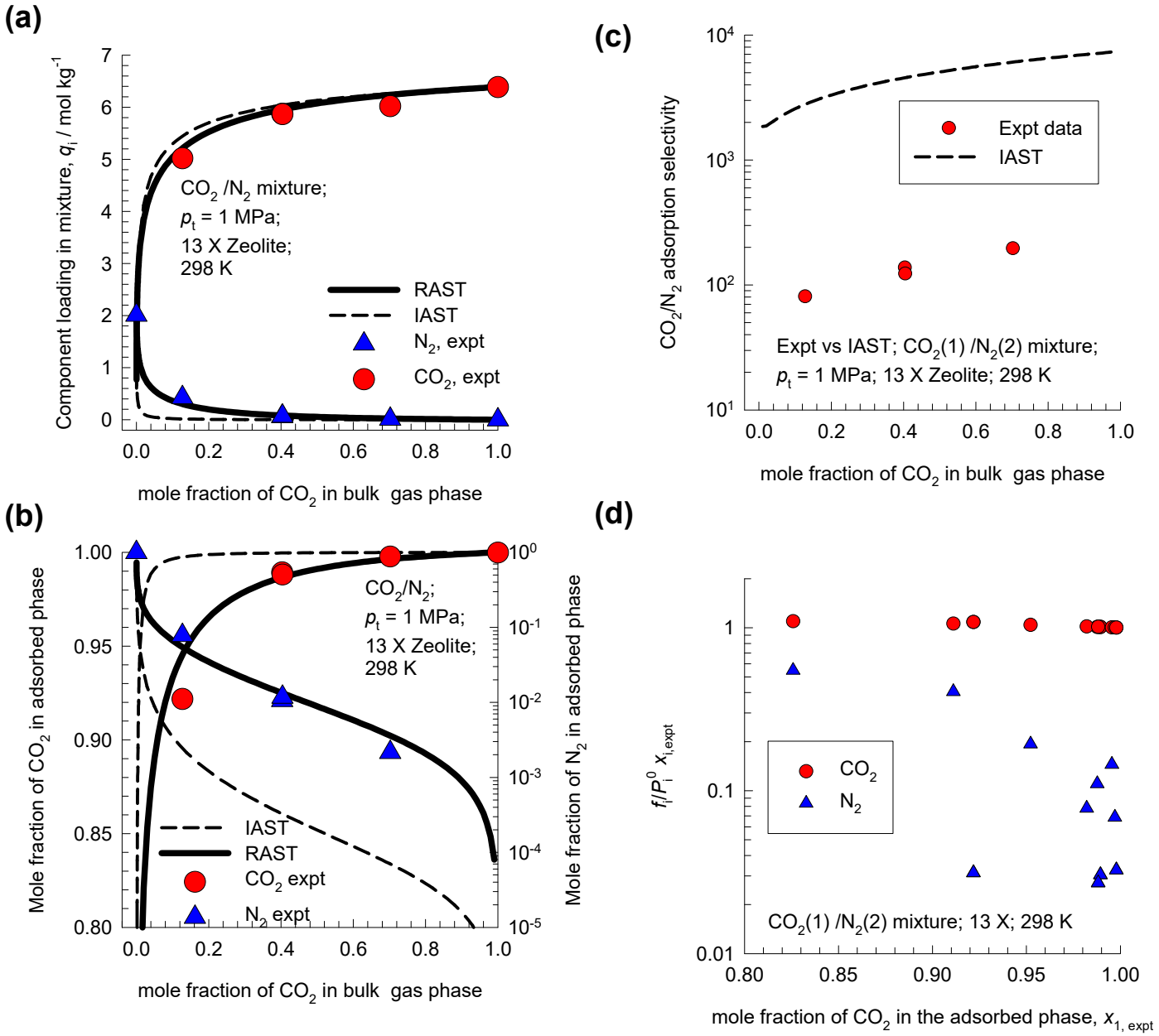

CO_2/CH_4 mixture adsorption in LTA-5A zeolite: Re-analysis of Mofarahi-Gholipour data

Figure S3

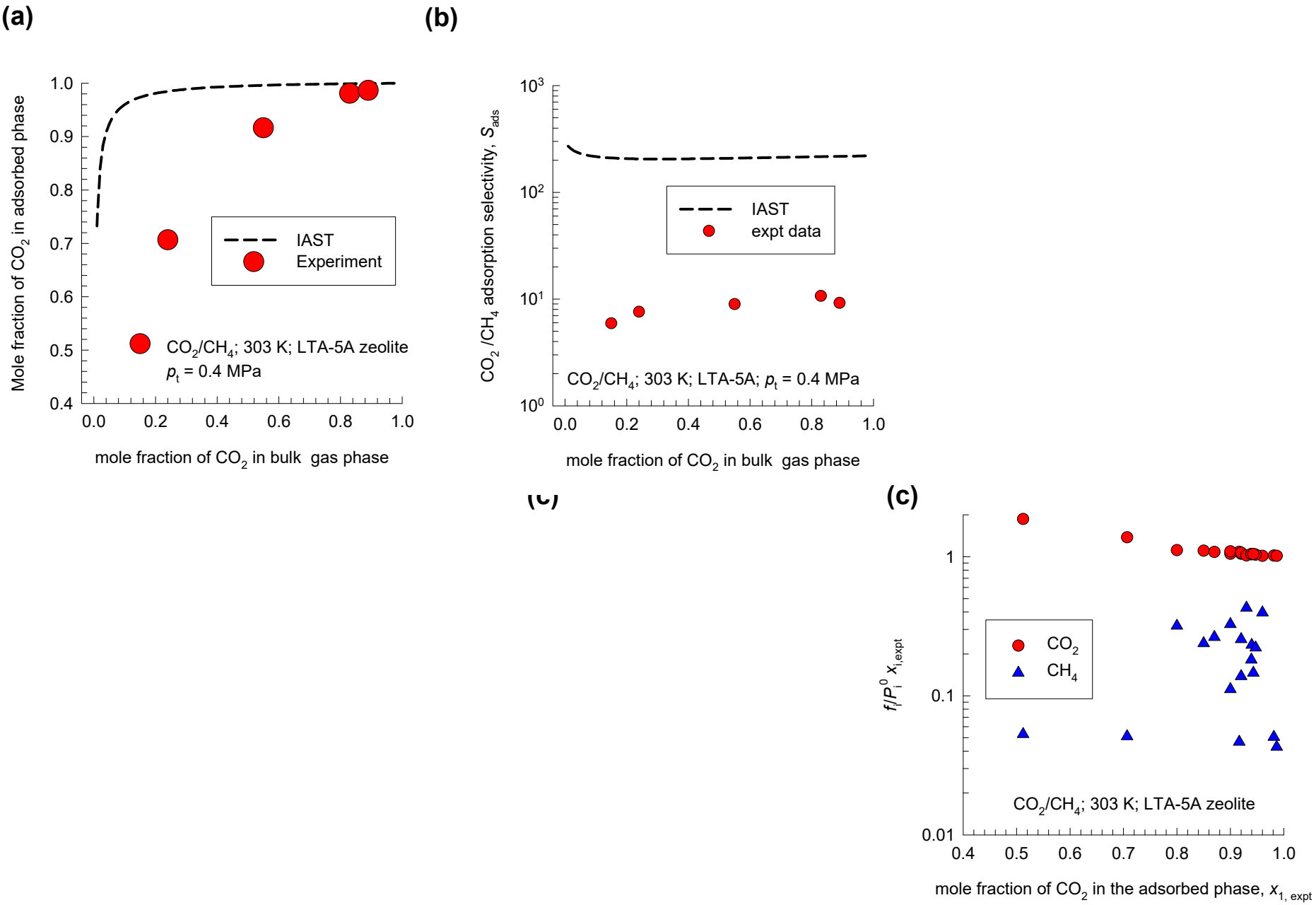

CO_2/C_3H_8 mixture adsorption in NaX zeolite: Costa data analysis

Figure S4

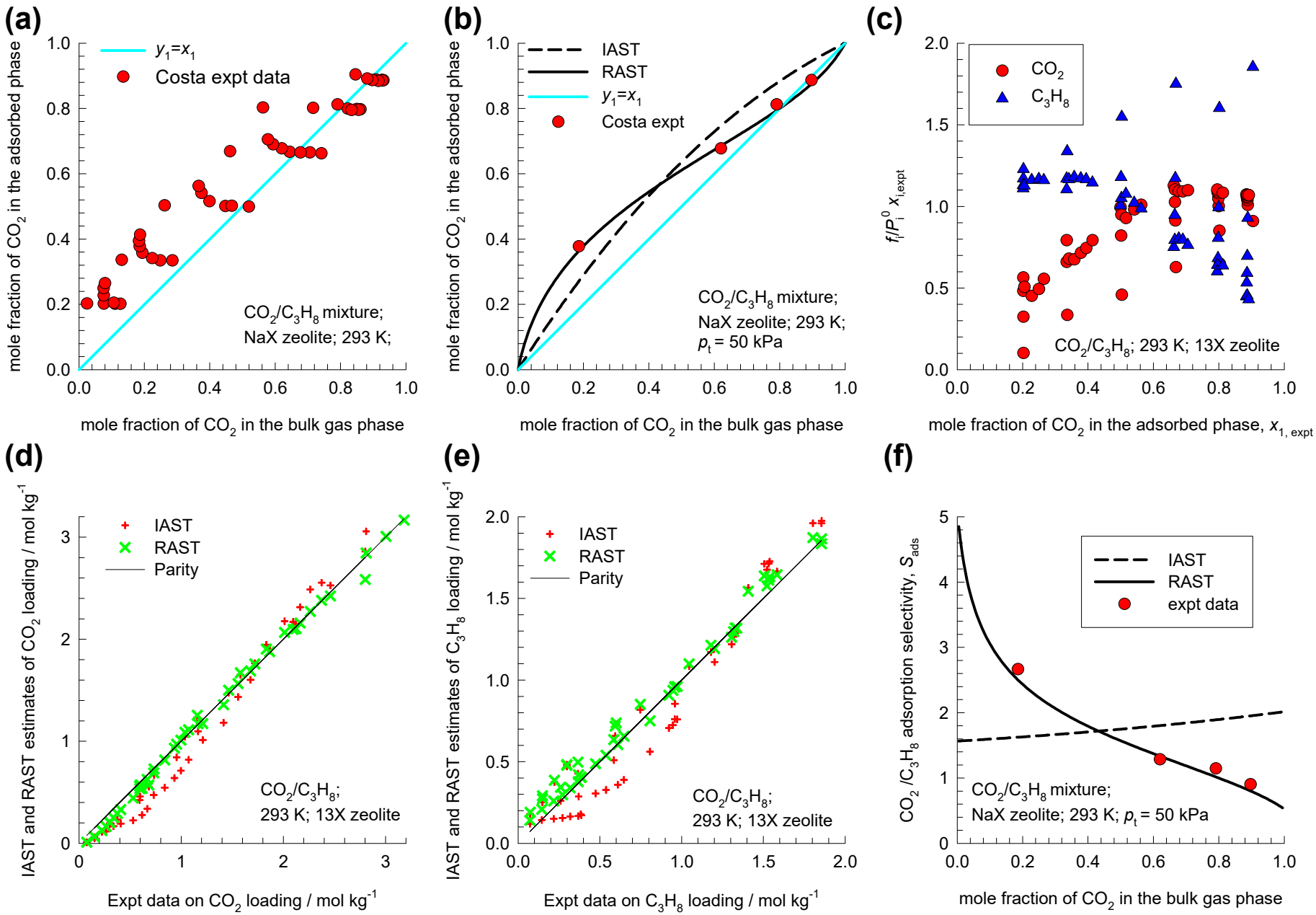

CO_2/C_3H_8 mixture adsorption in ZSM-5 zeolite: Calleja data analysis

Figure S5

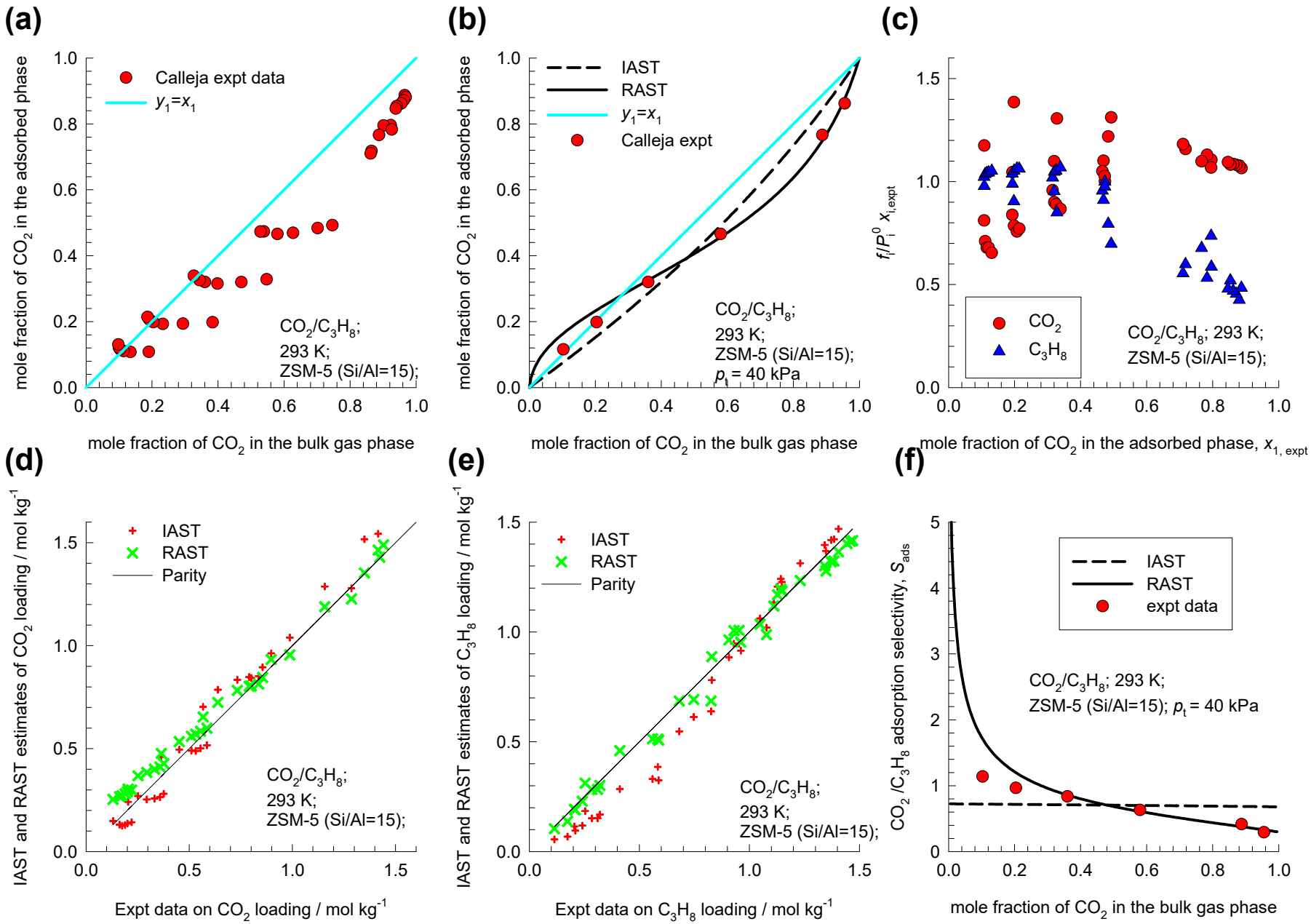

CO_2/C_3H_8 mixture adsorption in H-Mordenite: Talu-Zwiebel data analysis

Figure S6

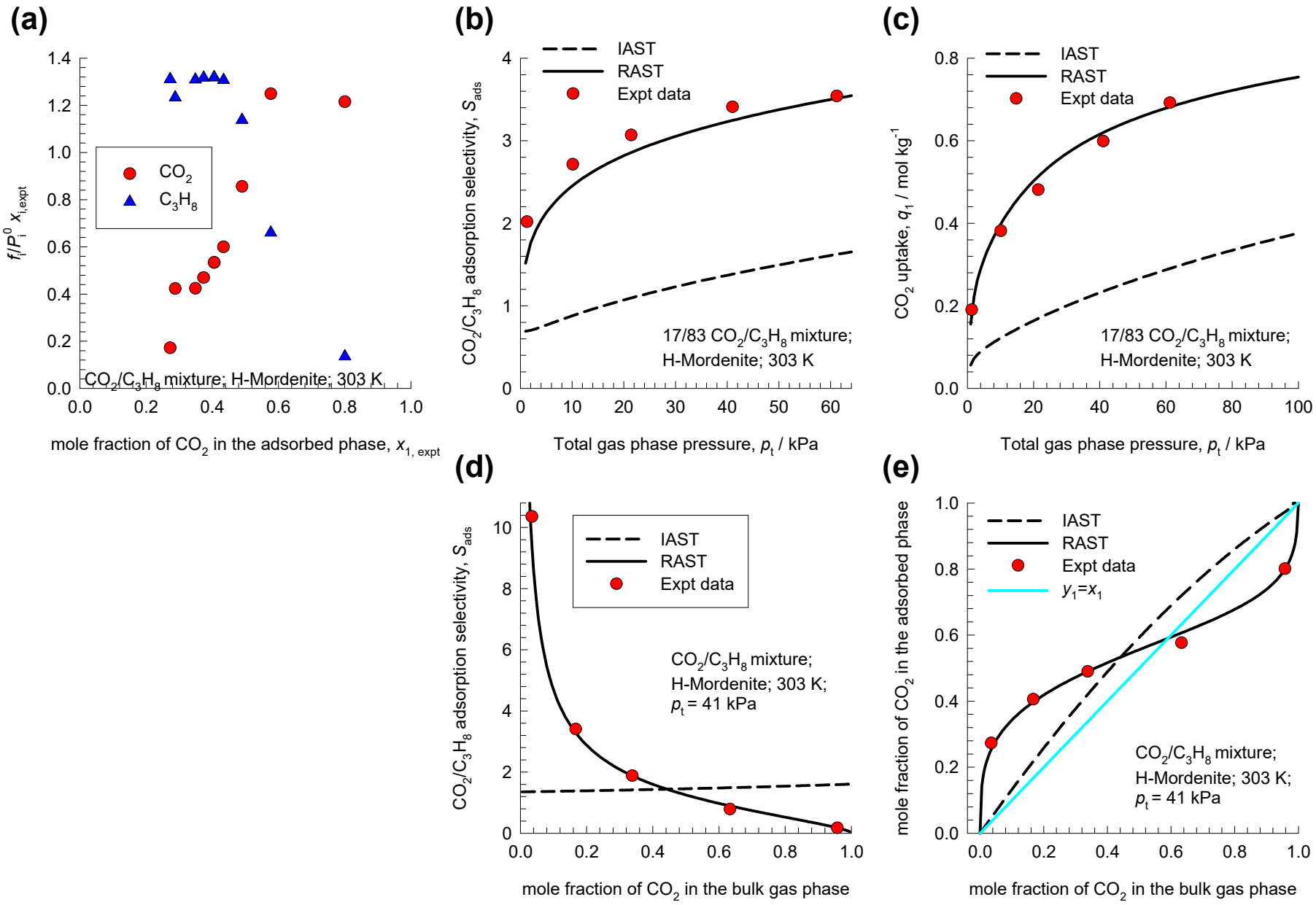

CO_2/CH_4 mixture adsorption in NaX (=13X) zeolite

Figure S7

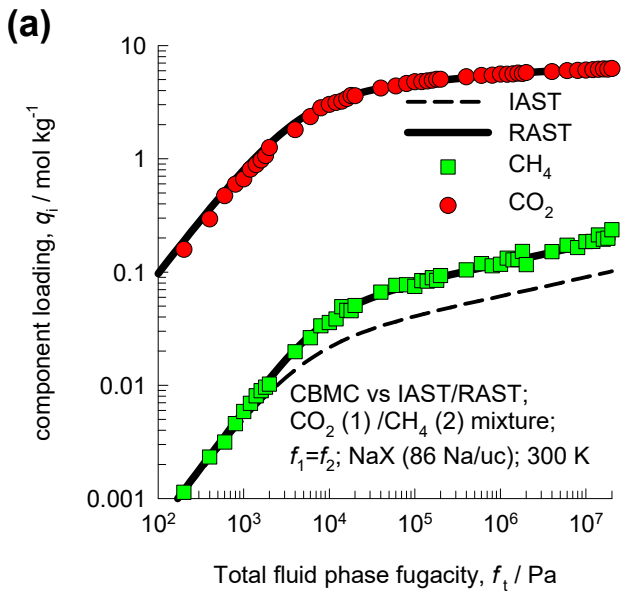

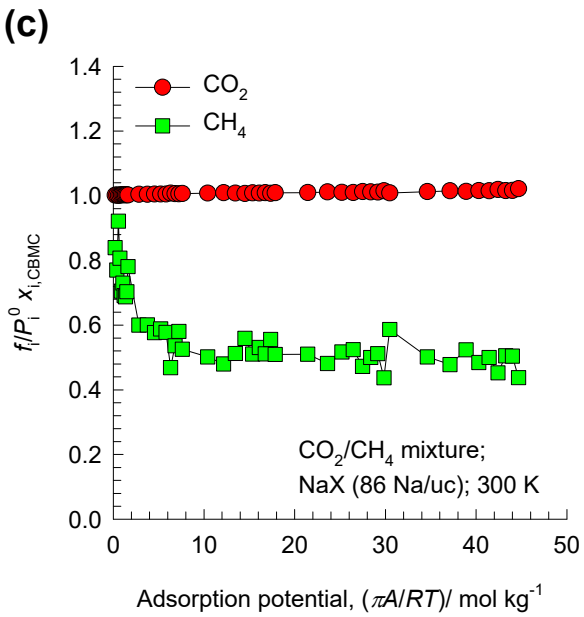

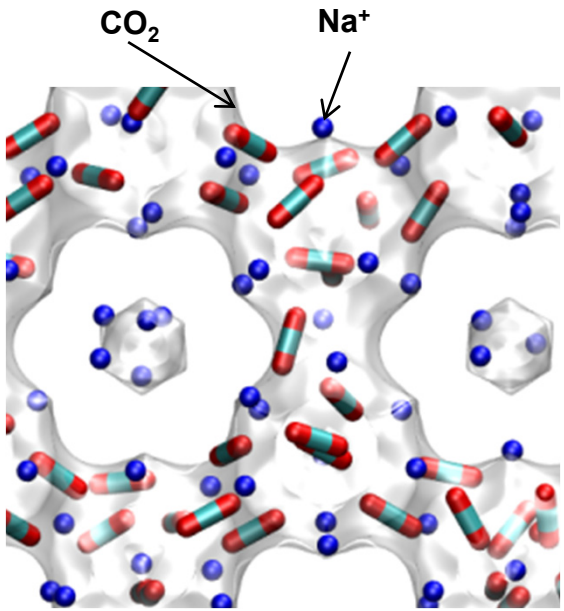

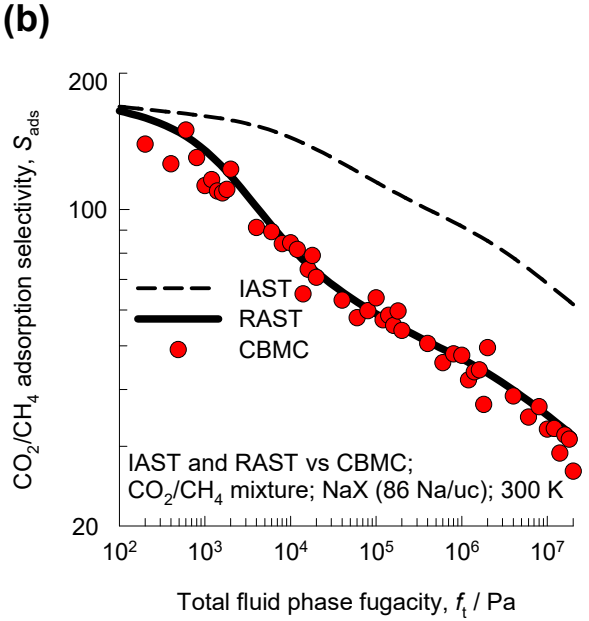

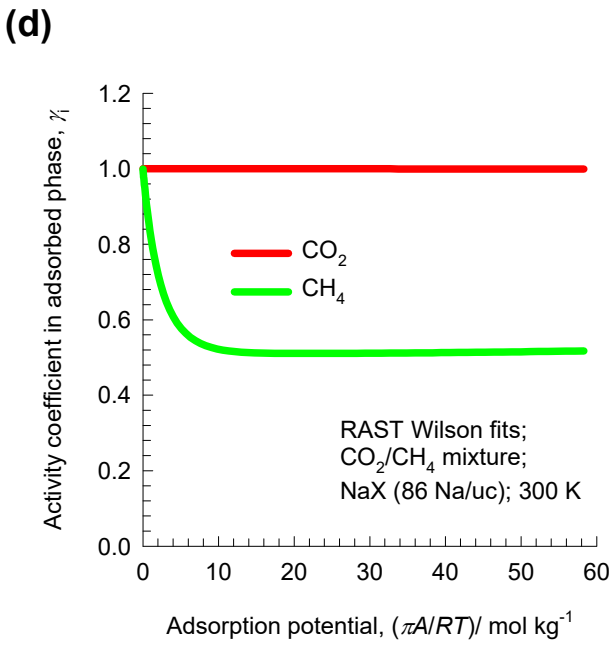

CO_2/N_2 mixture adsorption in NaX (=13X) zeolite

Figure S8

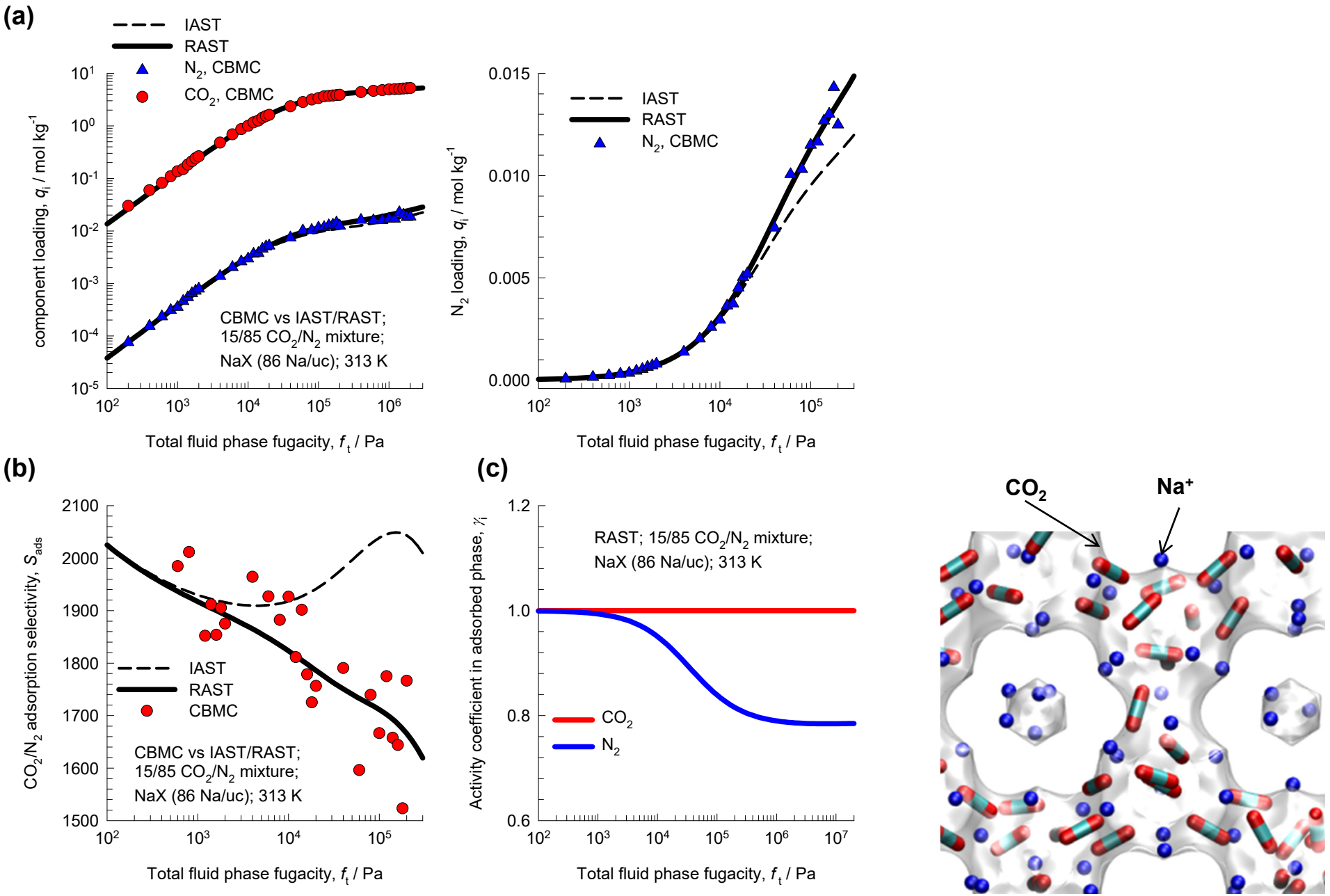

CO_2/H_2 mixture adsorption in NaX (=13X) zeolite

Figure S9

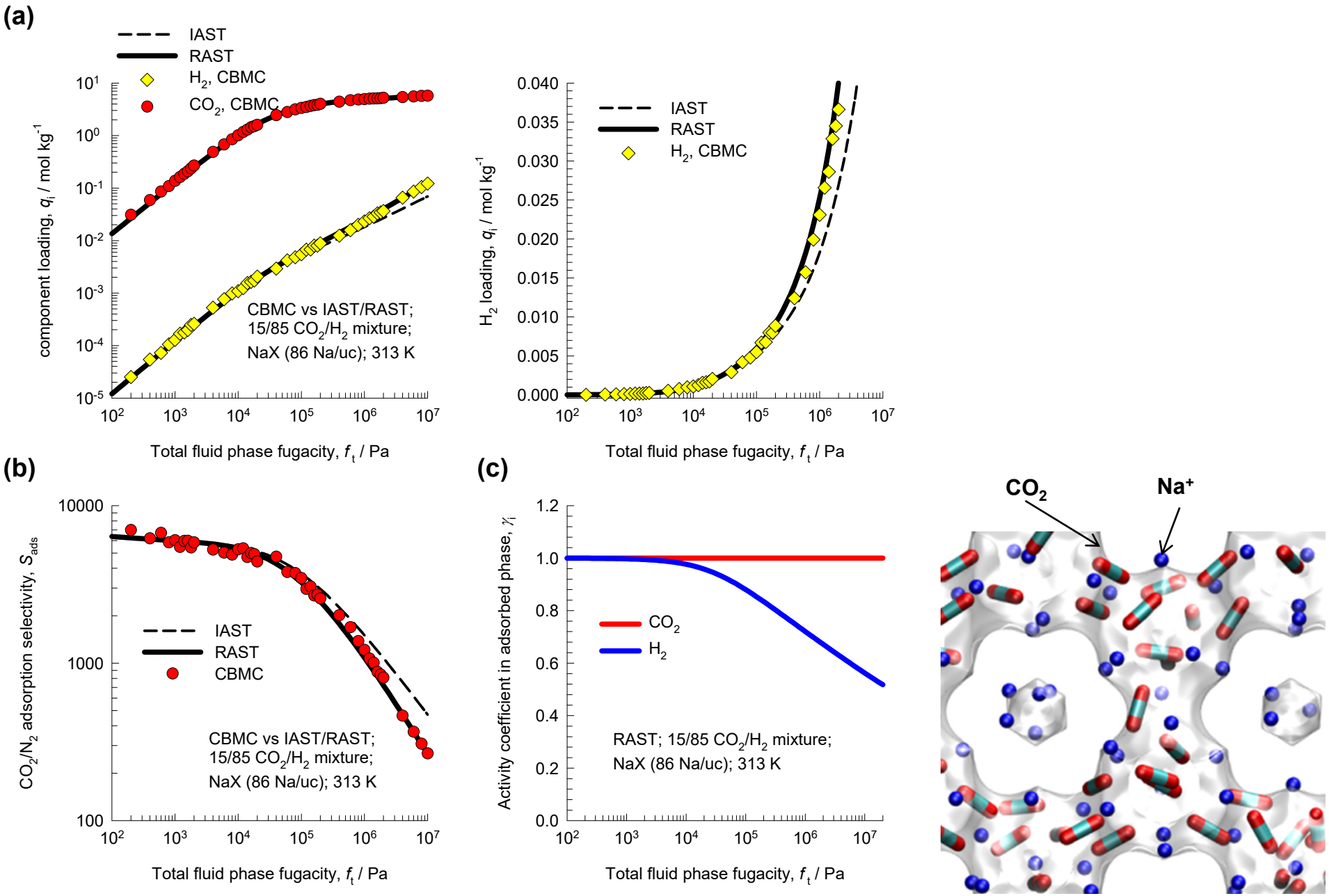

CO_2/CH_4 mixture adsorption in NaX, NaY, and all-silica FAU zeolite

Figure S10

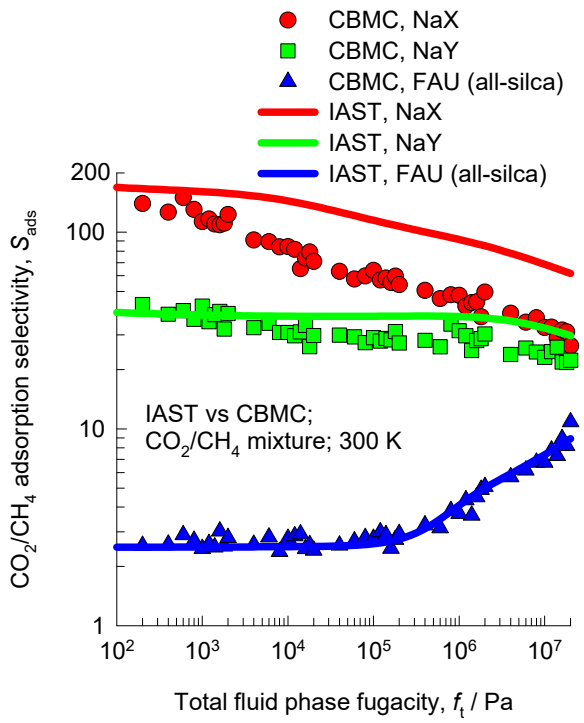

CO_2/C_3H_8 mixture adsorption in NaX (=13X) zeolite; $y_1 = 0.5$

Figure S11

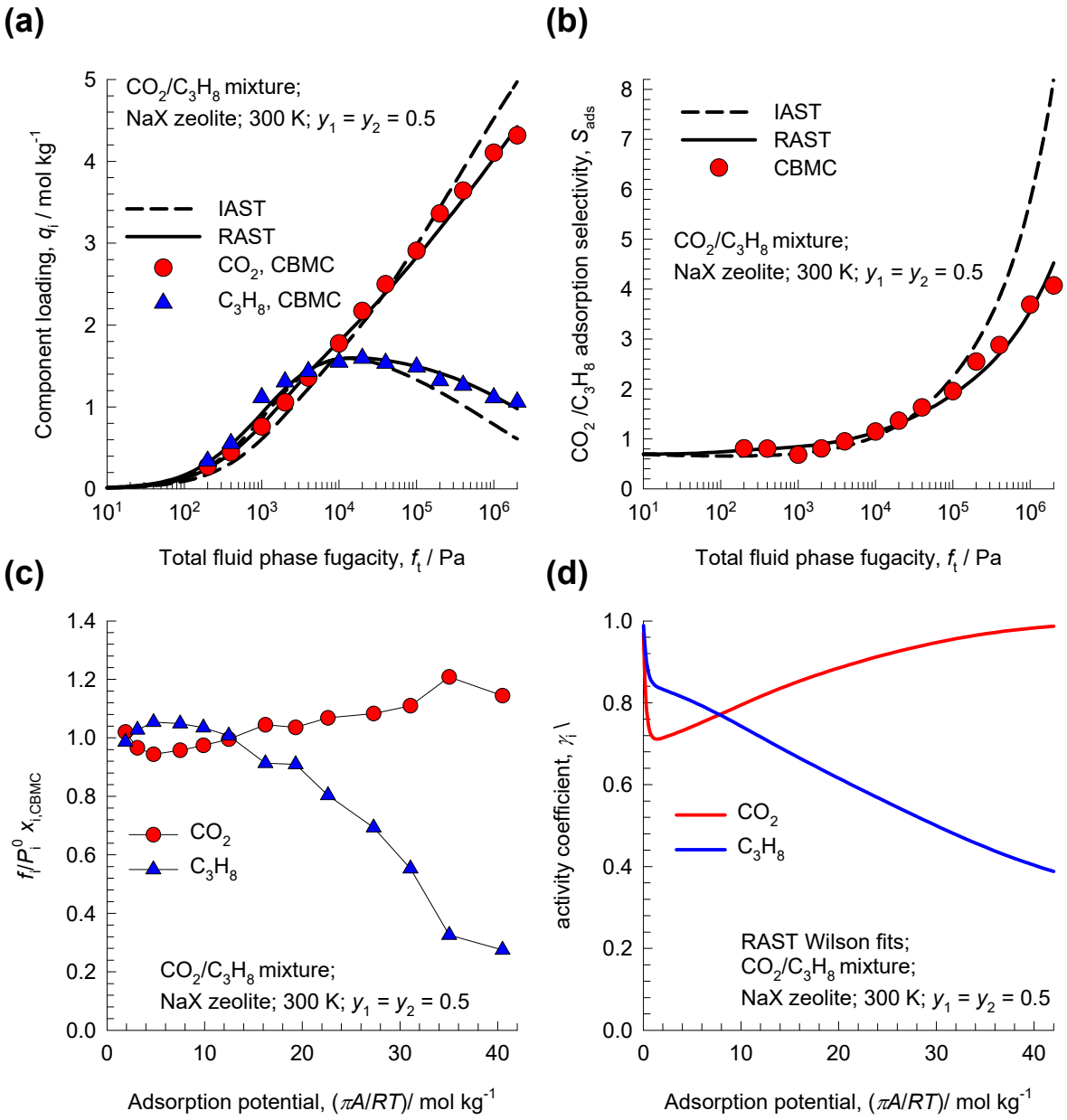

CO_2/C_3H_8 mixture adsorption in NaX (=13X) zeolite; f_t = 1 MPa

Figure S12

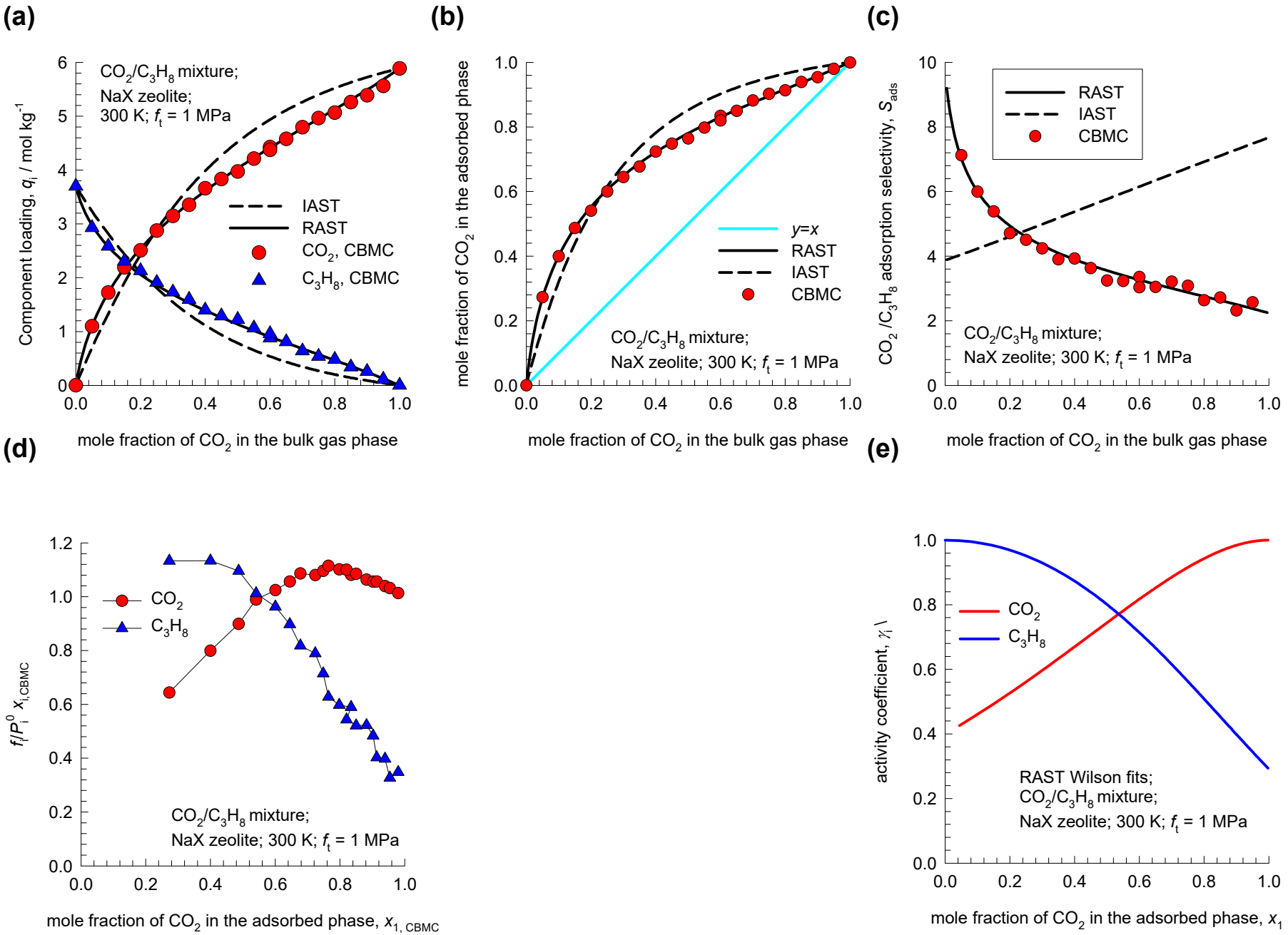

CO_2/C_3H_8 mixture adsorption in NaX (=13X) zeolite;
Snapshot for f_{CO2} = 50 kPa; f_{C3H8} = 950 kPa

Figure S13

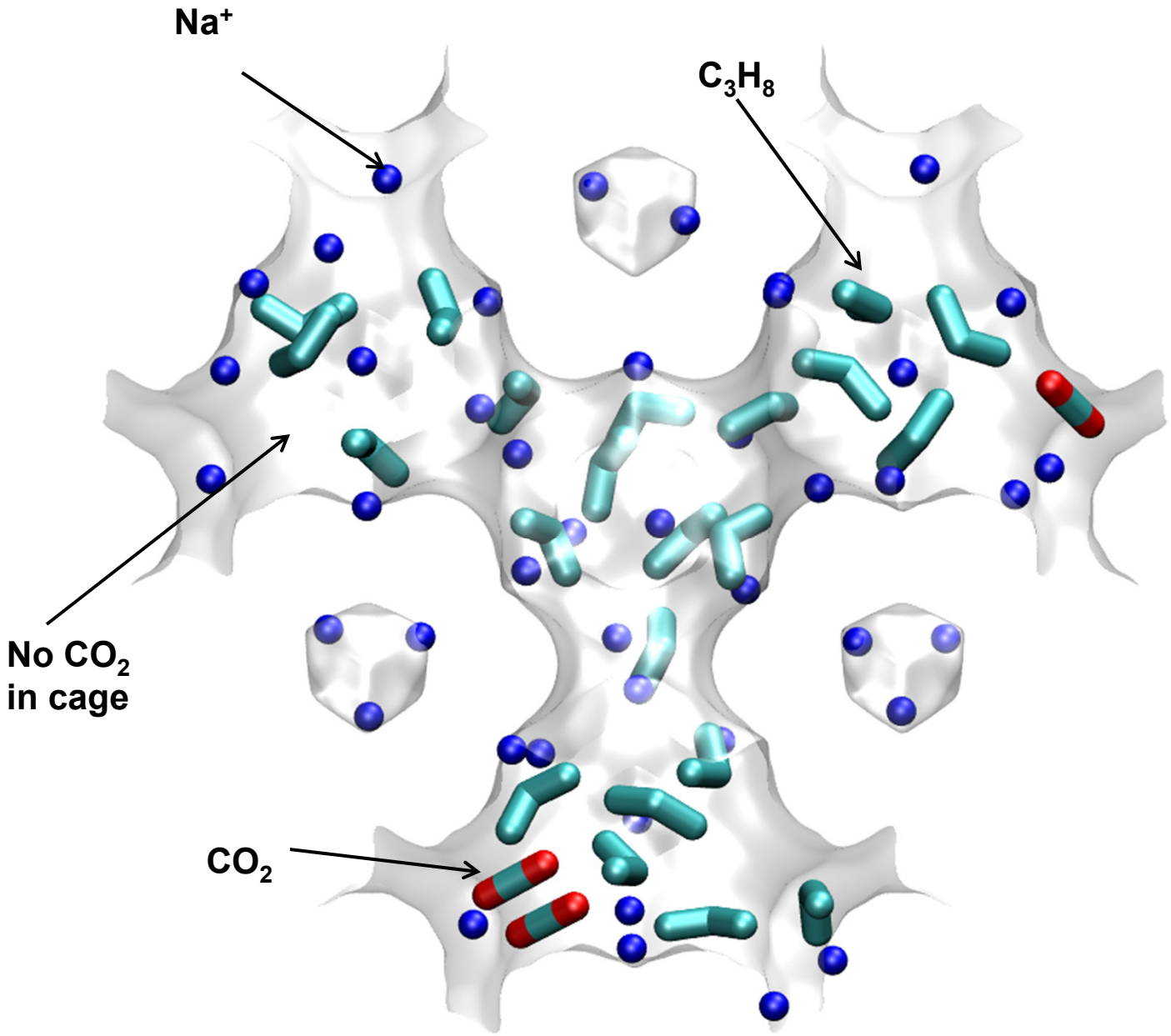

CO_2/C_3H_8 mixture adsorption in NaX (=13X) zeolite; Snapshot for f_{CO2} = 450 kPa; f_{C3H8} = 550 kPa

Figure S14

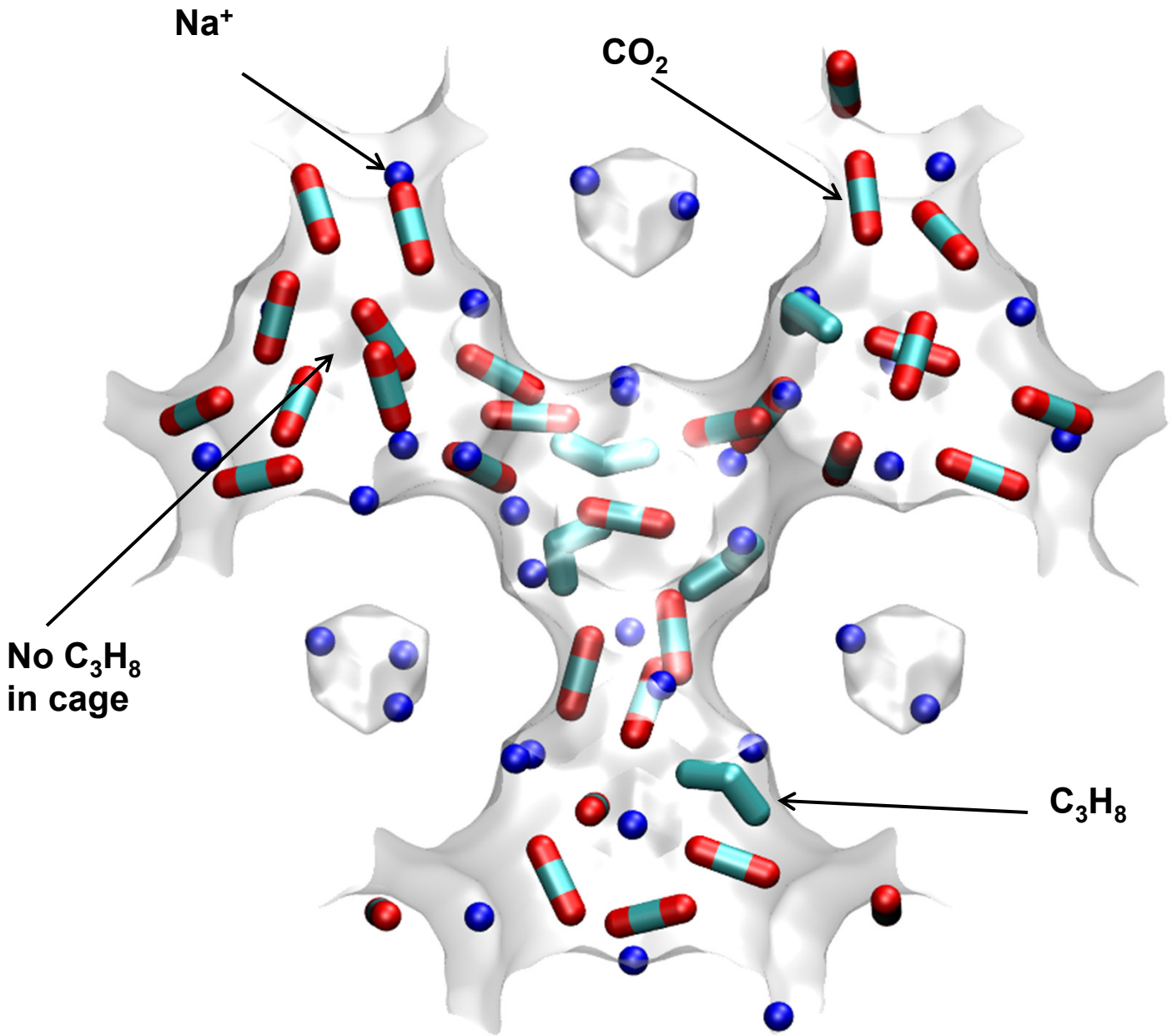

CO_2/C_3H_8 mixture adsorption in NaX (=13X) zeolite;
Snapshot for f_{CO2} = 500 kPa; f_{C3H8} = 500 kPa

Figure S15

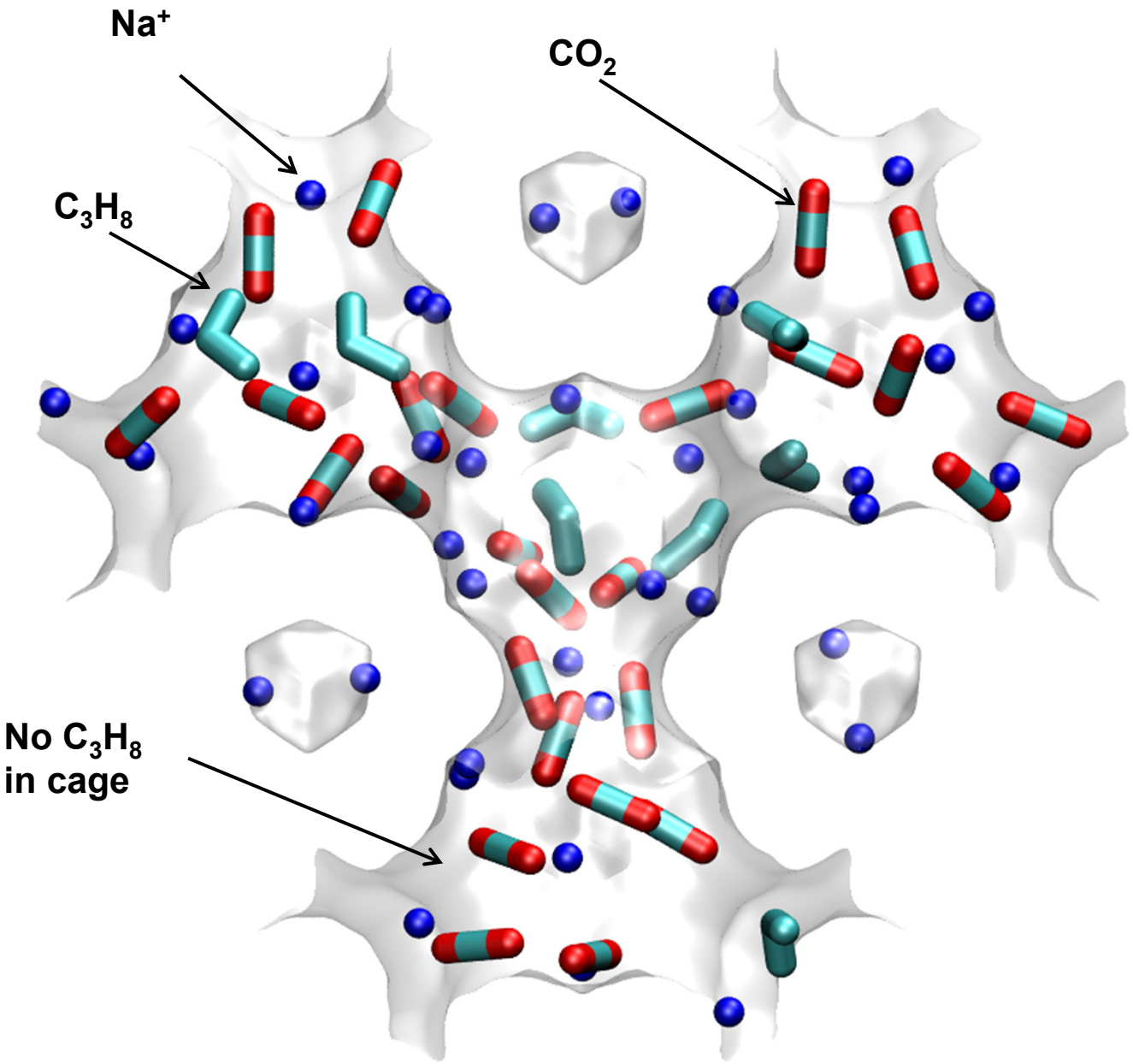

CO_2/C_3H_8 mixture adsorption in NaX (=13X) zeolite; Snapshot for f_{CO2} = 750 kPa; f_{C3H8} = 250 kPa

Figure S16

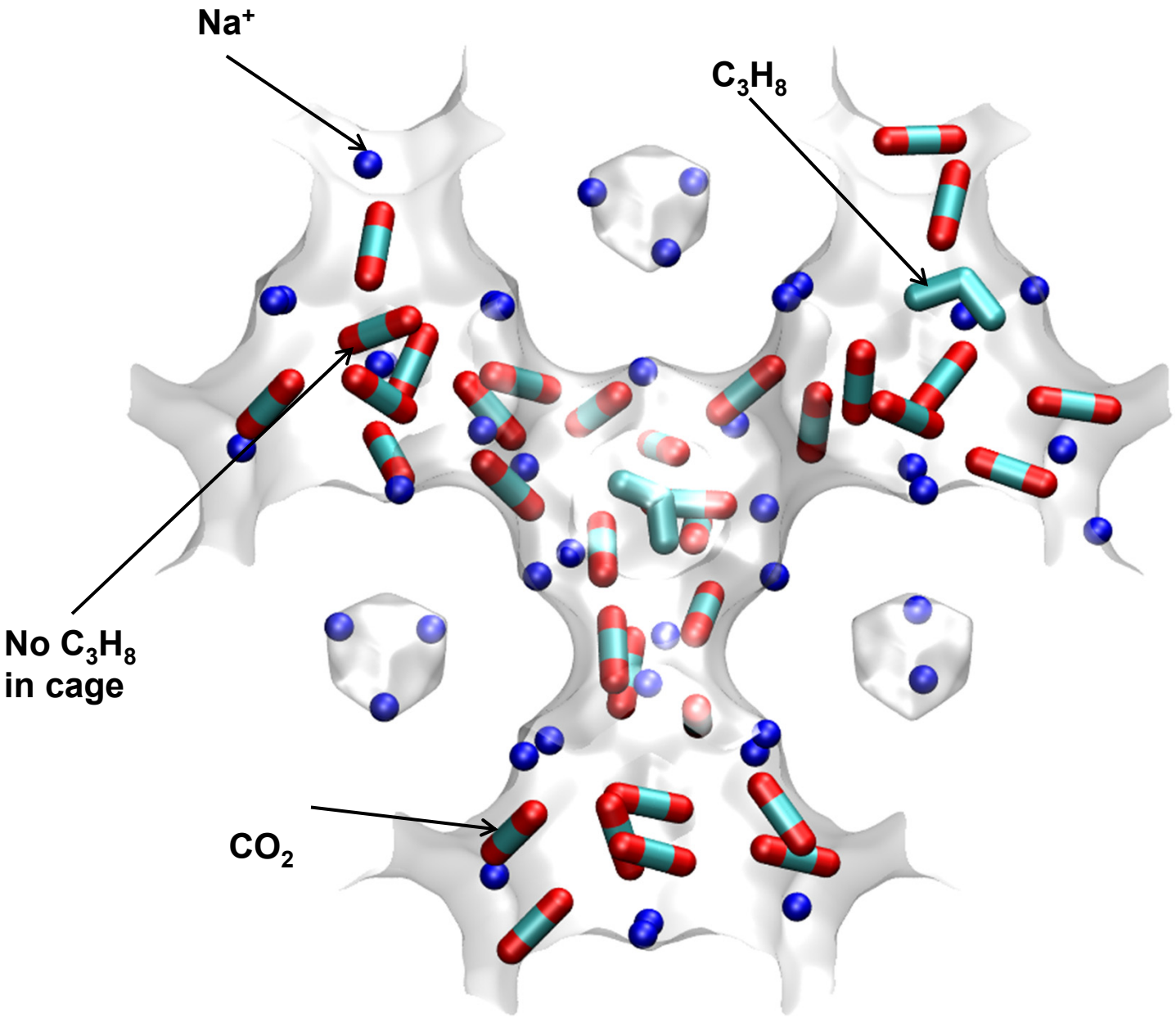

CO_2/C_3H_8 mixture adsorption in all-silica FAU zeolite

Figure S17

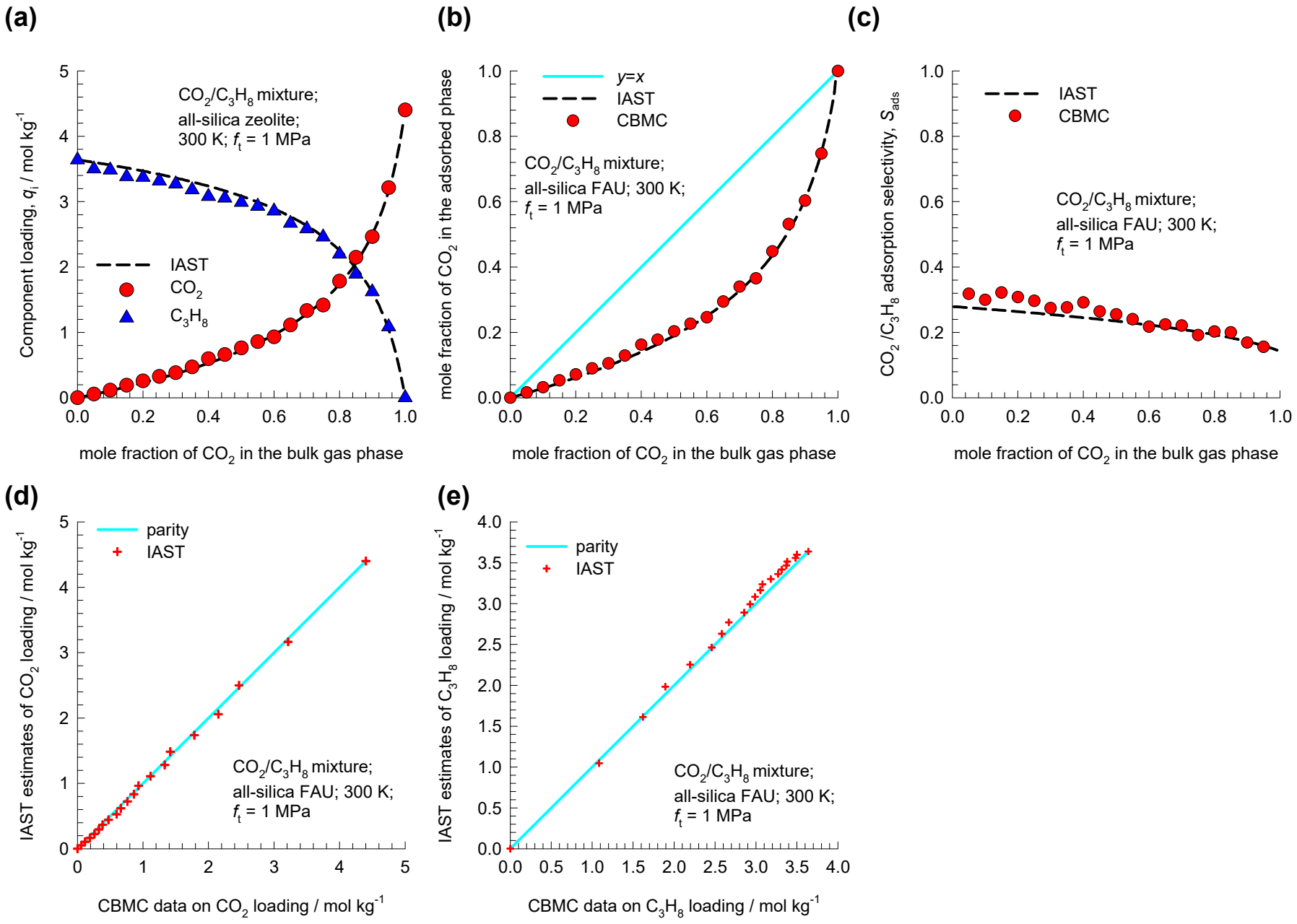

CO_2/C_2H_6 mixture adsorption in all-silica FAU zeolite

Figure S18

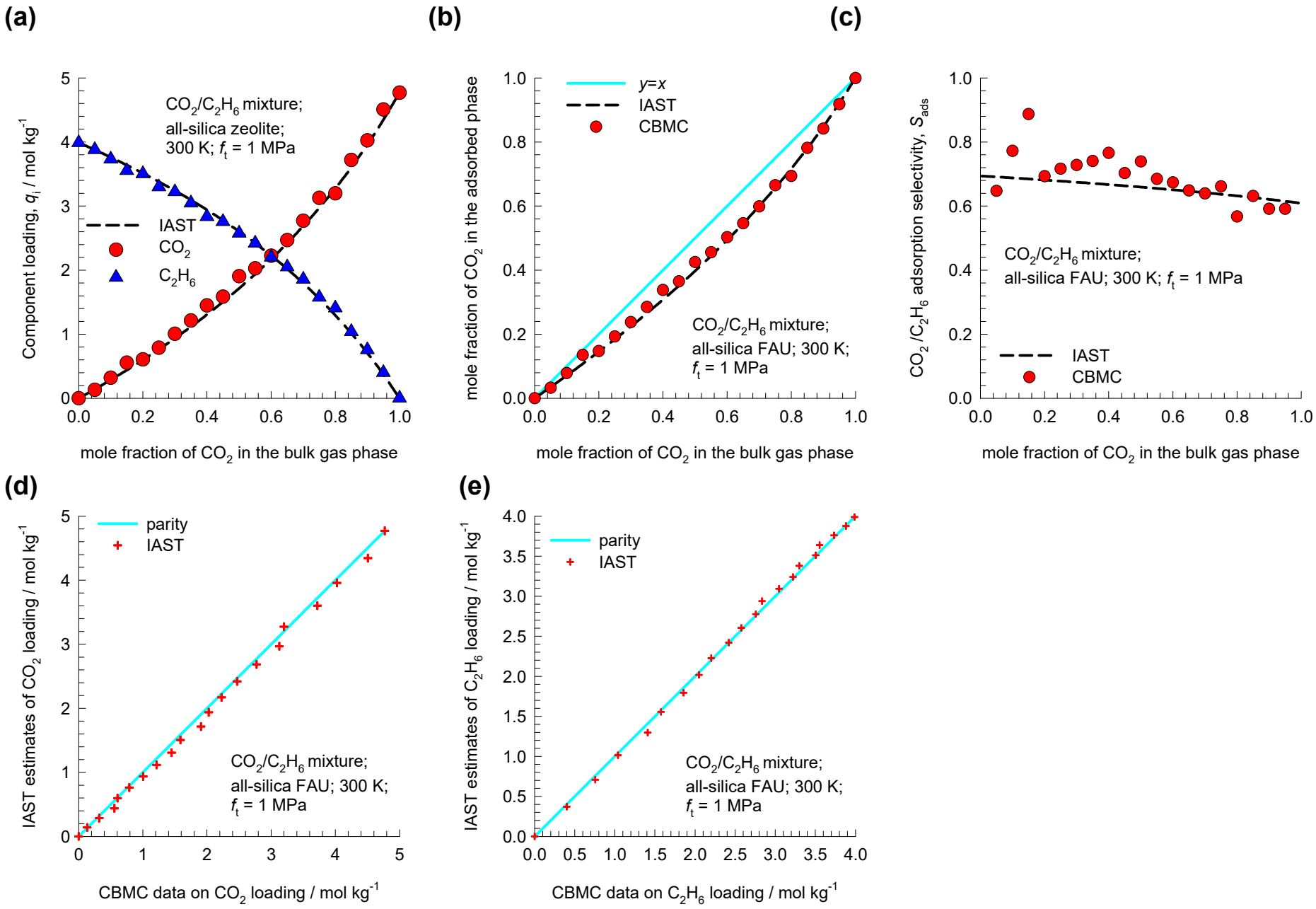

CO_2/C_3H_8 mixture adsorption in LTA-4A zeolite; f_t = 1 MPa

Figure S19

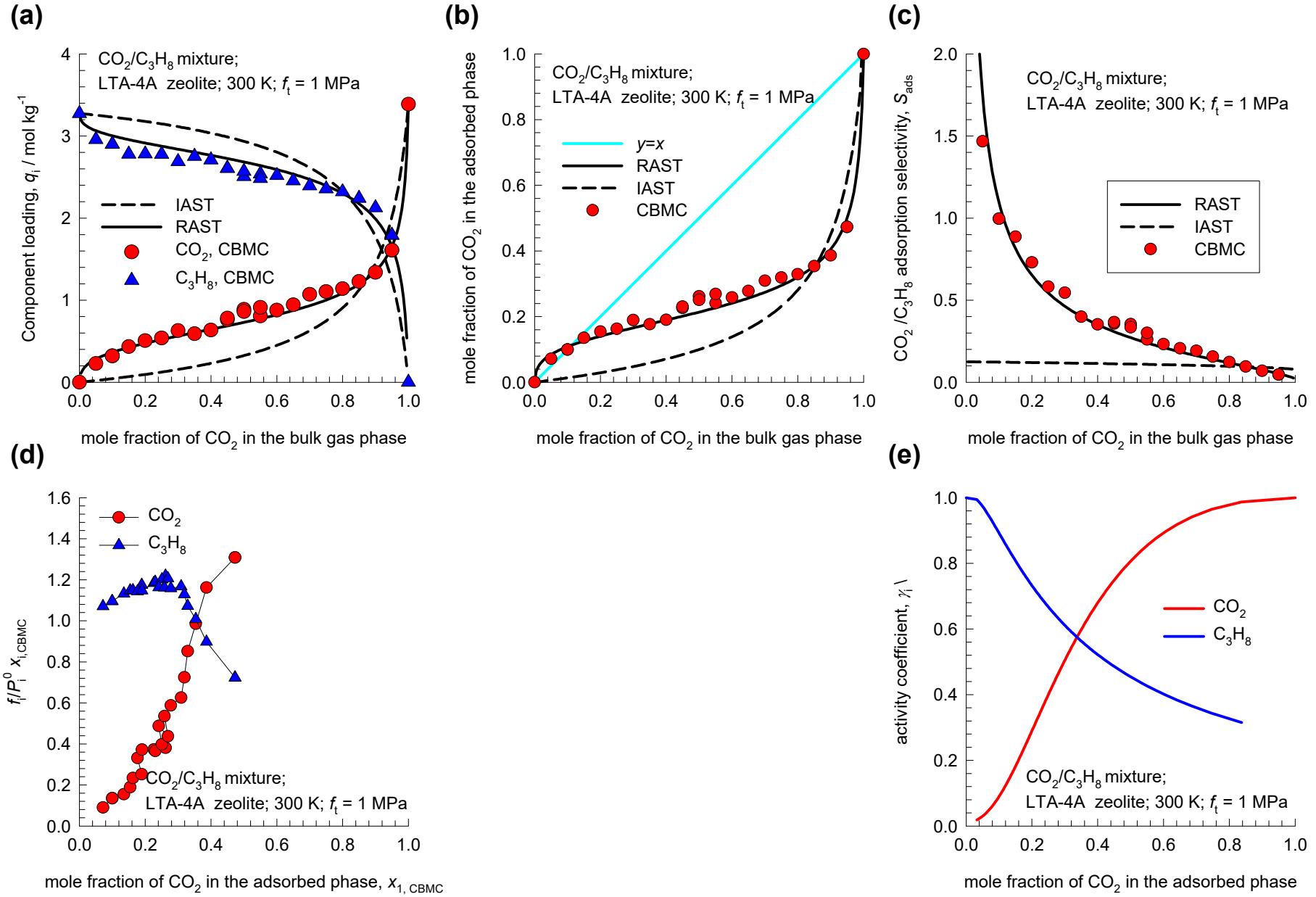

CO_2/C_3H_8 mixture adsorption in LTA-4A zeolite;
Snapshot for f_{CO2} = 250 kPa; f_{C3H8} = 750 kPa

Figure S20

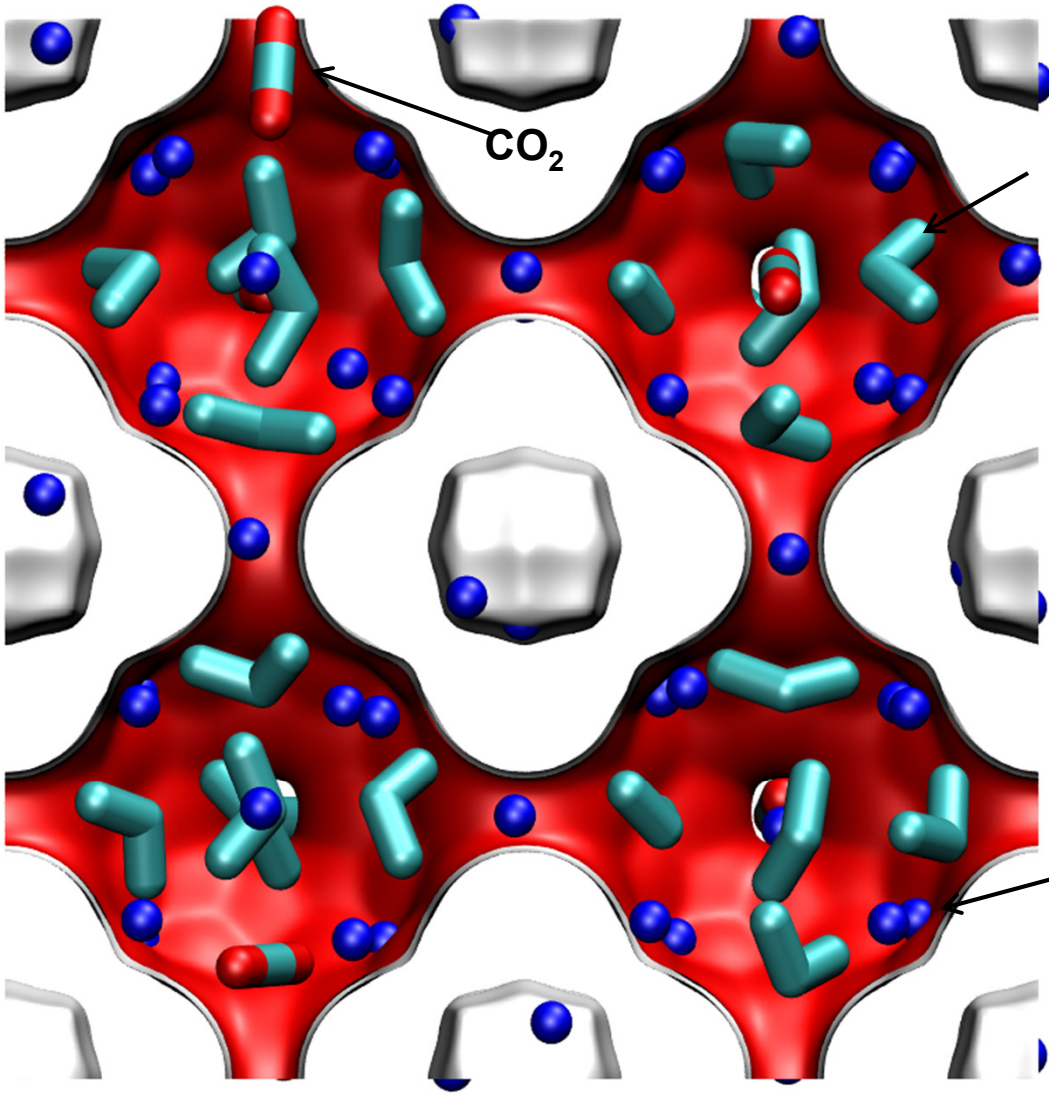

CO_2 only to be found in the window regions

CO_2/C_3H_8 mixture adsorption in LTA-4A zeolite; Snapshot for f_{CO2} = 550 kPa; f_{C3H8} = 450 kPa

Figure S21

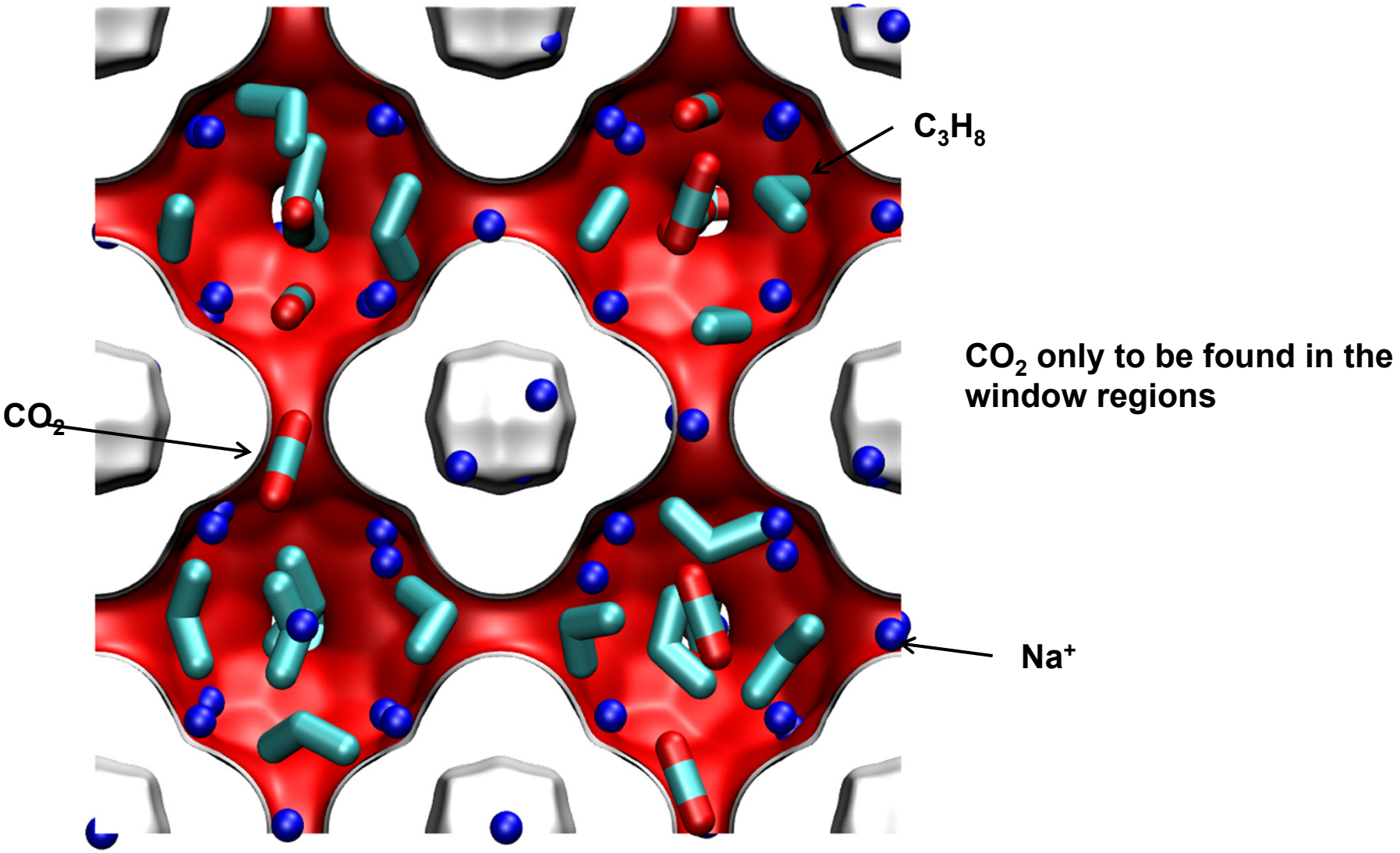

Figure S22

CO_2/C_3H_8 mixture adsorption in LTA-4A zeolite; Snapshot for f_{CO2} = 650 kPa; f_{C3H8} = 350 kPa

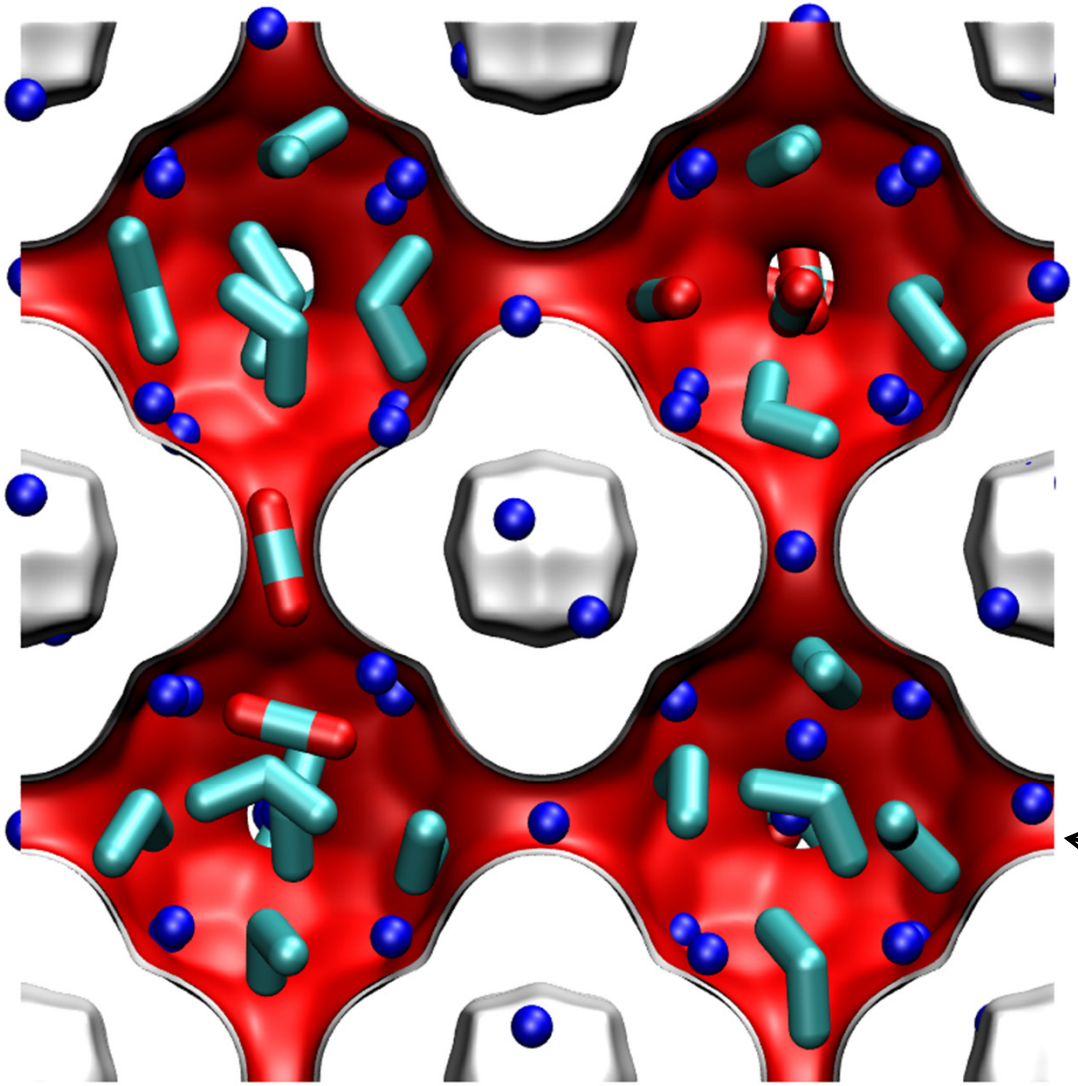

CO_2 only to be found in or around the window regions

Na^+

CO_2/C_3H_8 mixture adsorption in LTA-4A zeolite; Snapshot for f_{CO2} = 800 kPa; f_{C3H8} = 200 kPa

Figure S23

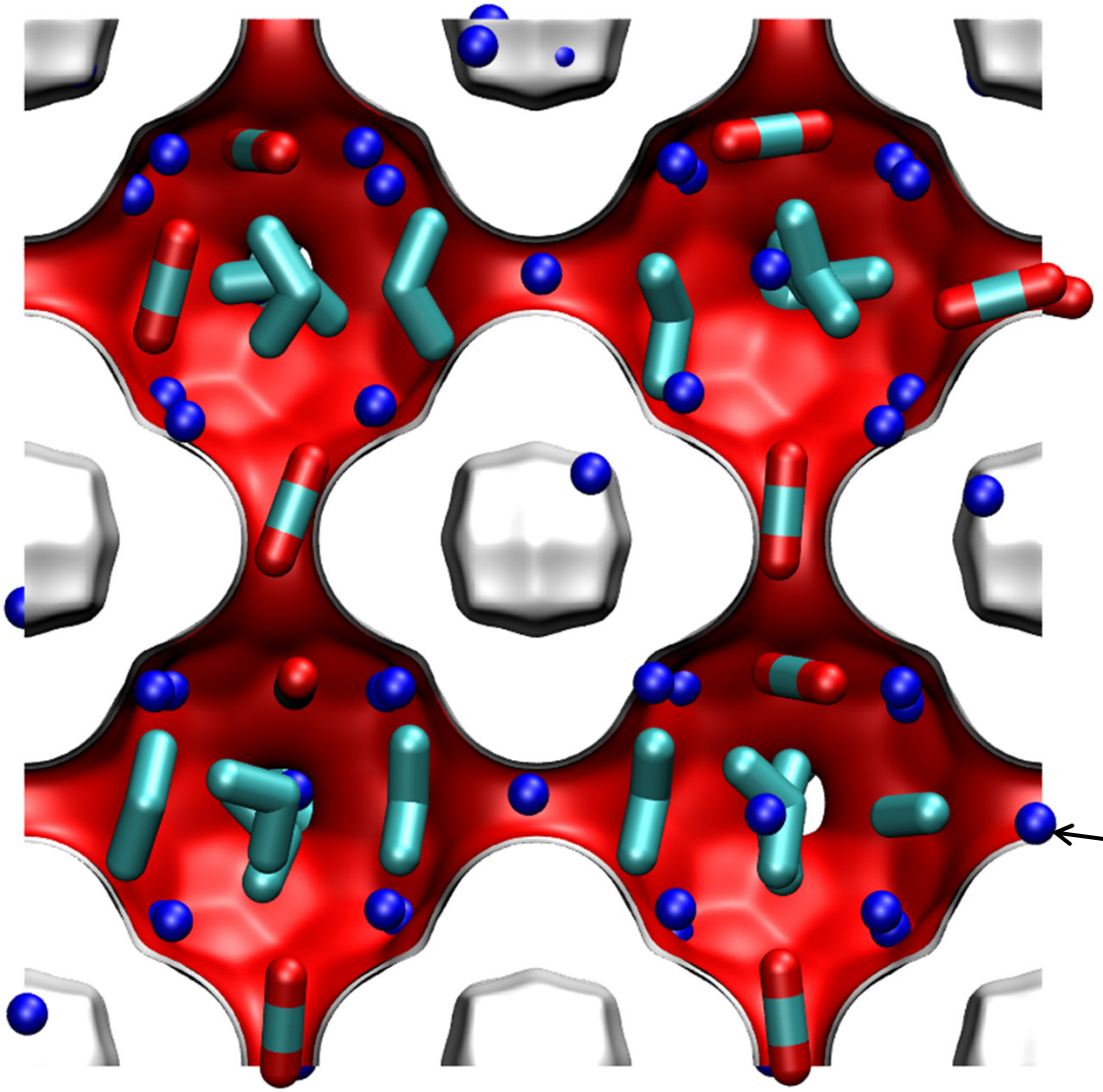

CO_2 only to be found in or around the window regions

Na^+

CO_2/C_3H_8 mixture adsorption in LTA-4A zeolite; Snapshot for f_{CO2} = 850 kPa; f_{C3H8} = 150 kPa

Figure S24

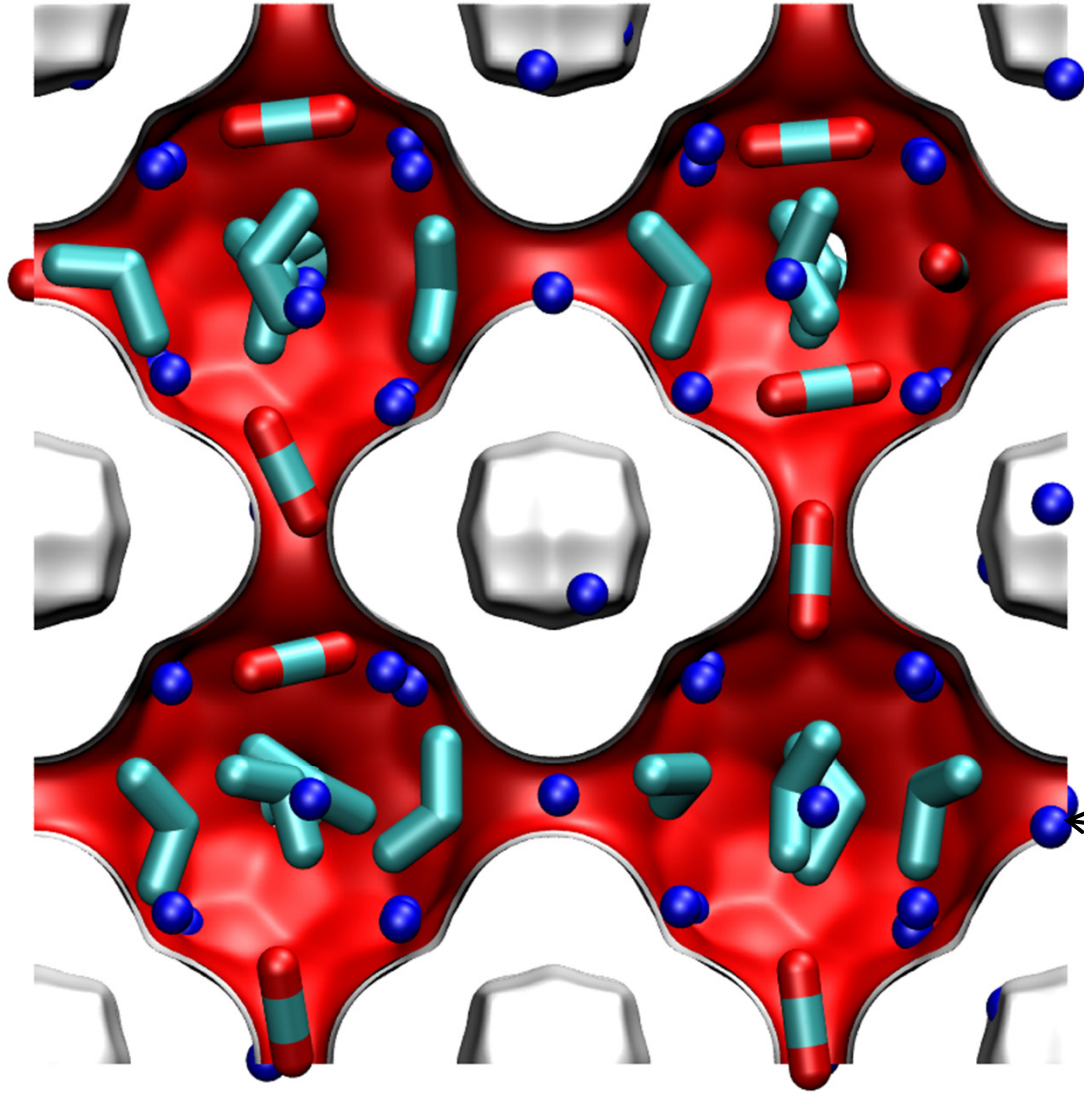

CO_2 only to be found in or around the window regions

Na^+